Imaging Pathological Stomach Tissue Using Polarization Second Harmonic Generation Microscopy

by

Hwanhee Jeon

A Thesis Submitted to
Saint Mary's University, Halifax, Nova Scotia
In Partial Fulfillment of the Requirements for
the Degree of Bachelor of Science with Honours

April 2023, Halifax, Nova Scotia

Copyright Hwanhee Jeon, 2023

Approved: _____
                   Dr. Danielle Tokarz
                   Supervisor

Approved: _____
                   Dr. David Dansereau
                   Reader

Date Submitted: April 14, 2023

Imaging Pathological Stomach Tissue Using Polarization Second Harmonic Generation Microscopy

by Hwanhee Jeon

ABSTRACT

Collagen is one of the main macromolecular components in the extracellular matrix (ECM), and its structure undergoes changes during cell differentiation and cancer progression in the tumour microenvironment. The main goal of the current study was to determine if polarization second harmonic generation (PSHG) analysis can be used to distinguish collagen structures in pathological from normal stomach tissue, and if it can be used to characterize the varying levels of adenocarcinoma differentiation. Using PSHG, we imaged normal and pathological stomach tissue samples which included well differentiated, moderately differentiated, and poorly differentiated gastric adenocarcinomas. Second harmonic generation (SHG) imaging is a non-linear optical microscopy technique that does not require staining of tissue samples due to the emission of SHG signals from intrinsic collagen fibers in the ECM. Therefore, it is less susceptible to observer variability compared to standard empirical staining techniques. For each sample image, PSHG analysis was performed to obtain ρ, a structural parameter associated with the degree of collagen disorder. Results showed that the mean ρ value was significantly greater in pathological tissue in patients compared to their adjacent normal tissue, which indicated a higher degree of structural disorder in cancerous tissue. There was a significant increase in mean ρ values from well differentiated to poorly differentiated adenocarcinoma. There was no significant difference in mean ρ values for groups that were closer to their degrees of tissue differentiation, such as between well differentiated and moderately differentiated, and between moderately differentiated and poorly differentiated adenocarcinomas. These findings suggest that there is greater disorder of collagen structure in the tumour microenvironment compared to adjacent normal tissue. Patients with poorly differentiated gastric adenocarcinoma are potentially ideal candidates for PSHG as a diagnostic technique.

April 14, 2023

Acknowledgements

I would first like to thank my supervisors Dr. Danielle Tokarz and Dr. Richard Cisek for providing me with the special opportunity to join their research group and for teaching me how to be a better researcher with their expert knowledge. This project would not have been possible without their continued support and patience. I would also like to thank MacAulay Harvey and Elisha Bennett for being such welcoming and encouraging lab members. They were always helpful and answered my countless questions about the microscope. The Tokarz Research Group's passion for learning has been a huge inspiration and I won't forget about all the memories I made at the lab this past year.

I would like to thank Dr. David Dansereau for being my thesis reader. His kindness and expert suggestions during the progress meetings provided me with a directed and clear approach to the project. I would also like to thank the Honours Seminar professors Dr. Anne Dalziel and Dr. Ellie Goud for their amazing seminar lectures and for providing me with continued guidance from the very start. In addition, I would like to thank the SMU Biology and Chemistry departments for their helpful feedback from the presentations throughout the year. To my fellow classmates from the Honours Class of 2023, thank you for being the best group of supportive individuals and for sharing this experience with me.

Lastly, I'd like to thank my family, friends, and loved ones. I found comfort and strength in their unconditional love and patience they've shown me throughout the journey.

Table of Contents

List of Figures

List of Tables

1. Introduction

1.1 Motivation

Gastric cancer is a disease that involves the proliferation and development of malignant cells originating from the stomach (Sitarz et al., 2018). Globally, it is the third leading cause of cancer death among males (Rawla & Barsouk, 2019). In 2020 alone, an estimate of 770 000 deaths were attributed to gastric cancer (Morgan et al., 2022). One of the reasons behind the high mortality rate is that patients are often diagnosed at an advanced stage since the disease is asymptomatic in its early stages (Sitarz et al., 2018). Being diagnosed at an advanced stage leads to a poorer prognosis, including a reduced survival rate (Sitarz et al., 2018). At an advanced stage, the median rate of survival is less than 12 months (Machlowska et al., 2020).

Gastric adenocarcinoma is the most common type of gastric cancer, representing 95% of cases (Schwartz, 1996). Adenocarcinomas arise from the glandular epithelial cells of the mucosa, which is the innermost layer of the stomach (Tetreault & Katz, 2012). Pathologists evaluate adenocarcinomas by observing the level of cell differentiation in stomach tumours. In developmental biology, differentiation is when a proliferating cell undergoes a phenotypic change to acquire a specialized function (Rakha et al., 2022). However, from the standpoint of histopathology, differentiation is strictly a morphological criterion used to compare the resemblance between cells from the neoplasm, which is an area of excess cell proliferation (Jögi et al., 2012).

A high level of differentiation describes neoplastic cells that share many similar characteristics and organization with the cells of origin (Jögi et al., 2012). A low level of differentiation describes neoplastic cells that have lost their structural organization and share few

physical features with the origin cells (Jögi et al., 2012). These varying levels of differentiation are important prognostic factors, in which a lower level of differentiation is associated with a higher level of tumour aggressiveness (Jögi et al., 2012). A study by Adachi et al. (2000) found that the 5-year survival rate of patients diagnosed with well differentiated gastric adenocarcinoma was about 10% higher than those with poorly differentiated gastric adenocarcinoma. Unfortunately, the level of differentiation of adenocarcinomas is a diagnostic challenge for pathologists because adenocarcinoma often shares architectural similarities to origin cells in normal tissue (Joo & Han, 2016). This provides a motivation behind researching new methods that aim to accurately diagnose and stage gastric adenocarcinoma. By doing so, pathologists can provide individualized treatment options based on the varying levels of differentiation to improve prognostic outcomes for cancer patients.

1.2 Current Limitations in Cancer Diagnosis

The standard technique in diagnosing gastric cancer is histological examination of stomach biopsies obtained using white-light upper endoscopy. Upper endoscopy involves inserting the shaft of an endoscope down the esophagus and into the stomach of the patient (Lee et al., 2015). The distal end of the endoscope illuminates the mucosal lining of the stomach with white light, allowing the endoscopist to identify abnormal areas of stomach tissue that they suspect are tumour growths (Lee et al., 2015; Tajiri & Niwa, 2008). The identification process involves distinguishing the morphological features of gastric lesions from normal gastric tissue (Kim et al., 2014). Key features of gastric lesions include red discolouration and ulceration of the mucosa, allowing endoscopists to locate and obtain biopsies of the lesions (Kim et al., 2014; Young et al., 2021).

Limitations in the upper endoscopy technique can result in additional biopsies being required. One such limitation is that foreign materials on the endoscope lens can prevent a high-resolution image from being obtained, leading to an imprecise observation (Park, 2015). Foreign materials on the lens can include food residue, bile, mucus and bubbles (Januszewicz & Kaminski, 2020). It is also important that endoscopists use a waterjet to remove excess contents in the stomach prior to endoscope insertion to improve visualization of the mucosal lining (Januszewicz & Kaminski, 2020; Park, 2015). Furthermore, the gastric lesion may be too large to fit within a single screen, requiring multiple images to be taken from different angles to avoid blind spots (Park, 2015). Although a standard minimum of at least 22 images to map out the entire stomach was proposed in Japan, this protocol is rarely followed in Western countries that follow the European Society of Gastrointestinal Endoscopy (ESGE) protocol (Januszewicz & Kaminski, 2020; Yao, 2013). ESGE protocol only requires four images during an endoscope examination for gastric cancer, lowering the chances of lesion detection (Yao, 2013). This demonstrates that obtaining biopsies through an upper endoscopy is highly dependent on the procedural training of the endoscopist as well as their ability to correctly interpret morphological changes and patterns of stomach tissue (Guo et al., 2008; Park, 2015). These limitations can have the potential to delay cancer diagnosis.

Once the biopsy is obtained, histological analysis by a pathologist is required for a final diagnosis (Guo et al., 2008). This involves examining a thin section of tissue on a microscope slide under a high-resolution light microscope (Slaoui & Fiette, 2011). Prior to examination, a fixative such as formalin preserves the components of the tissue by chemically cross-linking soluble proteins to structural proteins (He et al., 2012; Slaoui & Fiette, 2011). Tissue samples are then embedded in paraffin wax to precisely cut the samples with a microtome into sections

measuring about 4-5 μm in thickness (He et al., 2012). This allows light from the illuminator of the light microscope to pass through the sample for visualization (Knoblaugh & Randolph-Habecker, 2018).

Another critical step in microscope slide preparation is adding an exogenous dye to the tissue sections, which increases contrast between different cellular structures for visualization. Hematoxylin and eosin (H&E) is the routine stain used for histological analysis (He et al., 2012). For more than one hundred years, H&E staining has been regarded as the gold standard by pathologists (Keikhosravi et al., 2020). Hematoxylin stains nuclei dark blue whereas eosin, the counterstain, produces varying shades of pink, red, and orange for cytoplasmic organelles and for the extracellular matrix (Fischer et al., 2008).

Although histopathologists routinely use H&E to examine biopsies, variations in tissue staining and observer skill can present challenges to an accurate diagnosis. The intensity of the shades is affected by the duration of the fixation step with formalin (Tosta et al., 2019). Variations in colour prevent pathologists from accurately carrying out classification methods due to the reduced quality of texture and colours of intra-and extra-cellular features (Tosta et al., 2019). Since H&E is an empirical stain, final tissue samples are stained based on the preferences of the observer for analysis (Floyd, 2010). This can result in interobserver variability particularly if the H&E-stained samples need to be referred to a different institution (Floyd, 2010). Furthermore, H&E staining is limited in its sensitivity to the structure of collagen fibers because it only reveals the location and relative abundance of collagen in the tumour microenvironment (Rentchler et al., 2019). Since pathologists are confined in their ability to visualize collagen structures in great detail with H&E, well differentiated adenocarcinomas present a challenge in cancer diagnosis.

Using H&E staining, poorly differentiated cells in gastric adenocarcinoma can be clearly distinguished as they have very little glandular formation and the nuclei have a poorly cohesive structure (Arai et al., 2019). However, for well differentiated adenocarcinoma, the glands of the mucosa display either subtle or no nuclear atypia (Joo & Han, 2016). Under a light microscope using a low power of light, some of the few subtle architectural abnormalities that pathologists can look out for in the well differentiated subtype are branching and anastomosing glands. Branching glands are defined as structures that resemble the inverted shape of the letter "Y" and anastomosing glands produce structures that resemble the letters "H", "Y" or "X" (Ushiku et al., 2013). Well differentiated adenocarcinoma remains a diagnostic challenge because it requires pathologists to be attentive to the subtle architectural features and is thus highly susceptible to observational bias (Joo & Han, 2016; Ushiku et al., 2013).

The presented limitations at both the endoscopic and histopathologic levels of examination highlight the need for a standardized alternative for use in gastric cancer diagnosis. At the endoscopic level, obtaining accurate biopsies from the target gastric lesion is limited by subjective observations made by the endoscopist and by the technical restrictions of the endoscopic instrument. Final diagnosis is also affected by colour variations in H&E-stained specimen and by observer variability in pathologists. Since the accuracy of gastric cancer diagnosis is affected at these various stages, an additional confirmatory step that is standardized across institutions can reduce the incidents of additional biopsies being required. A quantitative approach can further tackle the current limitations in interobserver variability and can possibly tackle the problem of gastric cancer being too often diagnosed at an advanced stage (Sitarz et al., 2018).

1.3 Extracellular Matrix

One quantitative approach proposed by tumour imaging studies is to track changes in the components within the extracellular matrix (ECM), to characterize the degrees of differentiation in tumours during cancer progression. The extracellular matrix is a non-cellular scaffolding network present in tissue that is composed of an interlocking mesh of water, minerals, proteoglycans, and fibrous proteins (Frantz et al., 2010; Walker et al., 2018). The extracellular matrix has an essential role in supporting the function of surrounding cells by providing structural support and regulating or modulating biochemical cues that regulate cell-to-cell communication and tissue homeostasis (Frantz et al., 2010).

The ECM is a dynamic environment that undergoes continuous remodelling to maintain tissue homeostasis (Walker et al., 2018). Tissue homeostasis can be disrupted through a dysregulated mechanism of ECM remodelling, which is linked to pathological conditions, such as cancer (Barker et al., 2012). Dysregulated ECM remodelling results in abnormal changes to the orientation and arrangement of its components (Elgundi et al., 2019). This can be caused by aberrant post-translational modification of proteins (Elgundi et al., 2019; Walker et al., 2018). For example, the abnormal expression of members of the lysyl oxidase (LOX) family of enzymes is responsible for inducing structural changes to the ECM, that have been linked to the progression of malignant tumours (Barker et al., 2012).

The extracellular matrix is separated into two main matrices: the basement membrane and the interstitial stromal matrix (Figure 1). The basement membrane is a thin sheet of nonfibrillar collagens, laminins, collagen-producing fibroblasts, and proteoglycans that allow macromolecular components to interconnect within the sheet (Winkler et al., 2020). The basement membrane lines the basal side of epithelial and endothelial cells (Chang & Chaudhuri,

2019; Winkler et al., 2020). The interstitial matrix is the scaffolding and structural constituent

that connects with the basement membrane (Winkler et al., 2020). It is composed mainly of

fibrillar collagen, fibroblasts, proteoglycans, and elastin (Winkler et al., 2020). The porous gel-

like property of the stroma in the interstitial matrix also allows cells to interconnect with each

other (Winkler et al., 2020).
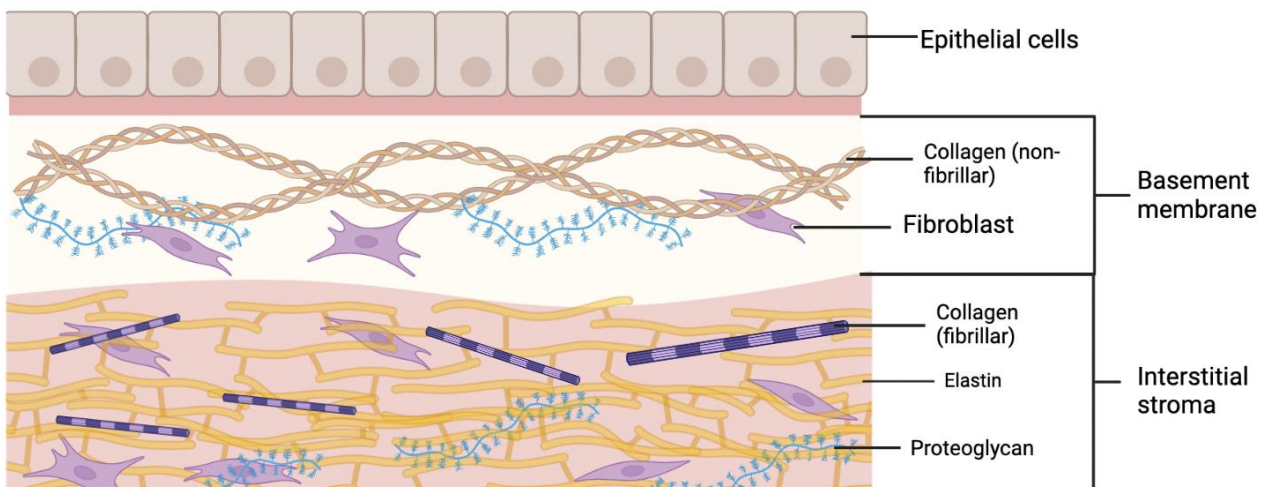
Figure 1. **A simplified diagram of the extracellular matrix and the main macromolecular
components within the matrices**. The epithelial cells are not part of the extracellular matrix. The
basement membrane is located on the basal side of the epithelial cells of the epithelium. The stroma of the
interstitial matrix connects with the basement membrane. This image was created using BioRender.

Remodelling of the basement membrane plays a key role in cell migration, growth and

differentiation in epithelial cancers, including gastric adenocarcinomas (Chang & Chaudhuri,

2019; Yin et al., 2009). The epithelial basement membrane acts as a physical barrier that

prevents carcinoma cells, which originated from the epithelium, from invading into the stroma of

the interstitial region (Chang & Chaudhuri, 2019). When the structural integrity of the basement

membrane is disturbed, primary tumour cells can undergo a malignant epithelial-mesenchymal transition and invade into the surrounding stroma (Elgundi et al., 2019).

Furthermore, dysregulated remodelling of the stroma of the interstitial matrix facilitates cancer progression. The tumour microenvironment characteristically has a stiffer and denser stromal network than the surrounding normal tissue (Bordoloi et al., 2020; Frantz et al., 2010). Changes in the components of the stroma contribute to the stiffness, which can then induce a series of further changes involving activated fibroblasts and tumour cells, initiating cell signalling events that generate more aggressive tumour cells (Nadiarnykh et al., 2010). Fibroblasts are elongated, spindle-shaped cells embedded in the ECM (Kalluri & Zeisberg, 2006). They are responsible for maintaining homeostasis of the ECM by secreting collagen and by regulating epithelial differentiation through growth factor secretion (Kalluri & Zeisberg, 2006). In the tumour stroma, fibroblasts become activated, which is associated with increased secretion activity of collagen, ECM-degrading proteases, and growth factors (Kalluri & Zeisberg, 2006). Therefore, tracking abnormal changes in the components of the ECM can serve as a tool to mark the progression of malignant tumours.

1.4 Collagen Remodelling in the Tumour Microenvironment

Collagen is the most abundant fibrous protein in both the basement membrane and interstitial matrix (Frantz et al., 2010). This makes collagen a key component to observe during dysregulated extracellular matrix (ECM) remodelling. A higher degree of ECM density and stiffness is a hallmark of the tumour microenvironment (Bordoloi et al., 2020). This can be

attributed to the increased activity of fibroblasts, which leads to an increased production of

collagen fibers in the ECM (Walker et al., 2018). The collagen fibers are then reoriented to

facilitate further stiffening of the stroma (de Wever et al., 2008; Walker et al., 2018). Stiffening

of the ECM can also be attributed to the increased expression of lysyl oxidase (LOX) enzymes

(Frantz et al., 2010). LOX enzymes are secreted by primary tumour cells and can induce cross-

linking of collagen molecules (Frantz et al., 2010). The underlying mechanism behind ECM

stiffening is that the N-terminus (end with a free amino group) and the C-terminus (end with a

free carboxyl group) of collagen molecules are cross-linked by LOX enzymes, within and

between collagen fibrils (Walker et al., 2018). A denser and stiffer ECM compresses intra-

tumoral blood vessels, which induces hypoxia and thus plays a tumour angiogenesis (Piersma et

al., 2020). Lysyl oxidase-like 2 (LOXL2) enzymes are part of the LOX enzyme family and they

are upregulated in gastric cancer (Peng et al., 2009). Upregulation of LOXL2 leads to an

excessive deposition of collagen which can promote cancer metastasis (Peng et al., 2009; Wu &

Zhu, 2015; Zhou et al., 2017).

These characteristics of collagen remodelling in the ECM are further observed in gastric

adenocarcinomas. A previous study by Zhou et al. (2017) observed gastric adenocarcinoma

tissue samples from patients using picrosirius red staining, which allows for selective

visualization of collagen under a light microscope. Zhou et al. (2017) found that collagen

deposition was increased in gastric adenocarcinoma samples compared to non-neoplastic

samples. Furthermore, immunohistochemistry was performed to confirm that there was an

increased number of collagen-producing activated fibroblasts and that expression of lysyl

oxidase-like 2 (LOXL2) was stronger in cancer than in non-neoplastic tissue (Zhou et al., 2017).

This finding suggests that dysregulated collagen remodelling occurs in tumour microenvironments and is related to the expression of LOXL2 enzymes.

Collagen organization in the ECM also varies across the different levels of differentiation in tumours. Previous studies observing ECM in oral squamous cell carcinoma demonstrated that in well differentiated tumour microenvironments, collagen fibers were oriented in a parallel arrangement and were packed densely due to collagen cross-linking (Bordoloi et al., 2020; Kardam et al., 2016). For poorly differentiated oral squamous cell carcinomas, collagen fibers were arranged haphazardly and displayed an increased amount of thinner collagen fibers as a result of activated fibroblasts (Bordoloi et al., 2020; Kardam et al., 2016). These results indicated that collagen structure becomes more disorganized in the ECM as cancer progresses (Kardam et al., 2016).

However, the aforementioned studies examining collagen organization in tumour microenvironments were limited since picrosirius red stained specimen were used to visualize collagen organization (Bordoloi et al., 2020; Kardam et al., 2016; Zhou et al., 2017). The methodology is limited since the stained features do not provide a complete, three-dimensional representation of collagen structure (Courtoy et al., 2020). Similar to the limitations in H&E, colours in picrosirius red stained specimen are affected by variability in staining protocol and interobserver variability, which prevents the reproducibility of results (Drifka et al., 2016).

1.5 Second Harmonic Generation Microscopy and its Application in Biological Imaging

In order to mitigate the issues associated with the use of picrosirius red staining such as variability in staining protocol and lacking a complete representation of collagen structure, we

used second harmonic generation (SHG) microscopy. SHG microscopy is a technique that does not require staining to visualize collagen ultrastructure in tumour microenvironments (Campagnola, 2011). Furthermore, SHG microscopy can provide quantitative data about collagen organization (Campagnola, 2011). These qualities of SHG microscopy demonstrate its applicability in imaging biological tissue and its potential use for cancer diagnosis in a clinical setting. Second harmonic generation is a second-order non-linear optical process that involves illuminating an appropriate medium, such as biological tissue, using an incident laser beam (Green et al., 2017). A second harmonic generation signal is emitted from the medium when two photons interact simultaneously in the medium and are converted to a single photon with twice the energy of the initial photons (Campagnola, 2011). This makes SHG a frequency doubling process, in which the single newly generated photon is twice the frequency of the incident laser light frequency (Li & Liu, 2010).

SHG has advantages over other multi-photon microscopy techniques, such as two-photon-excitation fluorescence (TPEF) for imaging biological tissue (Campagnola & Loew, 2003). Figure 2a demonstrates that TPEF involves absorption of the incoming energy and a Stokes shift during the relaxation from an excited state. Since the absorbed energy is released as heat in the Stokes shift, there is a risk of photobleaching using TPEF (Pantazis et al., 2010). In TPEF, photobleaching occurs when fluorescent probes no longer have the ability to fluoresce due to the finite lifetime of the excited state (Campagnola & Loew, 2003). As a result, target structures within the tissue can no longer be visualized (Vanheusden et al., 2020). Furthermore, absorption of light in TPEF can result in toxic by-products, which is harmful to live specimen for in-vivo imaging purposes (Icha et al., 2017; Pantazis et al., 2010). When fluorescent molecules

used in TPEF absorb light, they can react with oxygen and produce reactive oxygen species (ROS), which can lead to cell damage and death (Icha et al., 2017).

Conversely, energy is not deposited into the sample when imaging using the SHG microscopy technique (Campagnola, 2011). This is due to SHG making use of a virtual state rather than partially losing energy during relaxation from an excited state (Campagnola & Loew, 2003). Figure 2b below shows that the initial photons interact in a virtual state and consequently energy is not lost through absorption by the system. Figure 2b also shows that SHG is a frequency doubling process where the frequency of the newly generated photon (ω) is twice the incident frequency (ω_i), so that $\omega = 2\omega_i$.
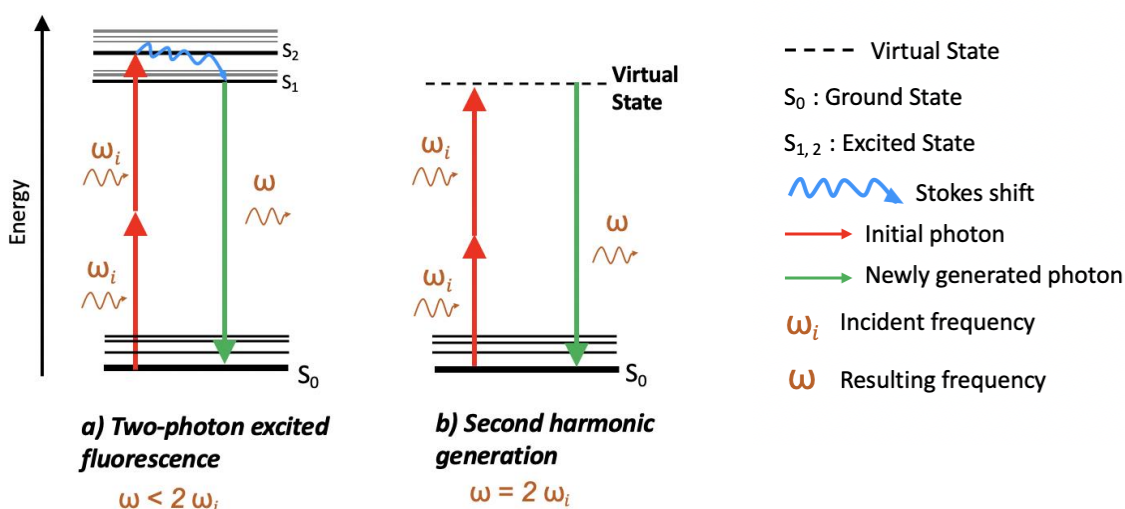
Figure 2. **A Jablonski energy diagram comparing the non-linear optical processes of A) two-photon excitation fluorescence and B) second harmonic generation**. **A)** Energy is absorbed and lost to the system during relaxation from an excitation state to a lower energy state through a Stokes shift. The resulting frequency (ω) is less than the combined incident frequencies of the two initial photons ($2\omega_i$). **B)** Two photons interact at a virtual state rather than an excited state, which does not involve absorption and loss of energy to the system. The resulting frequency of the generated photon is equal to the combined incident frequencies of the two initial photons. Figure adapted from Boyd (2008).

SHG is an ideal method for imaging biological tissue particularly for in-vivo

applications, since the absence of a Stokes shift means that there is no absorption of energy by

the sample (Figure 2). This eliminates the risks of photodamage and phototoxicity to samples

(Campagnola & Loew, 2003; Pantazis et al., 2010). Another advantage of using SHG

microscopy is the degree of tissue penetration that can be achieved. Since SHG microscopy uses

near-infrared lasers as the incident beam source, longer excitation wavelengths (~1045 nm) allow

for deep tissue penetration up to 500 μm (Bueno et al., 2017; Campagnola et al., 2002). This can

be achieved without photodamage, which has further in-vivo tissue imaging applications (Bueno

et al., 2017; Campagnola et al., 2002).

The strength of SHG signals from the second-order non-linear optical process is

characterized by the second-order non-linear optical susceptibility tensor, $\chi^{(2)}$ (Boyd, 2008;

Hermans et al., 2017). Only certain micro- and macro-molecular structures that exhibit $\chi^{(2)}$ can

emit SHG signals (Nadiarnykh et al., 2010). SHG imaging thus requires an appropriate medium

(Nadiarnykh et al., 2010). An appropriate medium which emits SHG signals must have non-

centrosymmetric characteristics (Pantazis et al., 2010). This means that both the molecular

structure and the macroscopic arrangement of the molecules in the medium lack a generalized

mirror symmetry (Pantazis et al., 2010).

Collagen is one of the few biological materials intrinsic in tissue that has a non-

centrosymmetric assembly at the molecular level (Kim et al., 2000; Williams et al., 2005).

Collagen is a right-handed bundle composed of three left-handed helical α-chains (Shoulders &

Raines, 2009). Therefore, the non-centrosymmetric structure of collagen is attributed to its

overall triple-helical structure that lacks inversion symmetry (Shoulders & Raines, 2009). Since

the intrinsic collagen in tissue emits strong SHG signals, samples can be visualized without

adding any fluorescent probes, which is required for TPEF, or exogenous stains like H&E and picrosirius red, which is required for light microscopy (Campagnola, 2011; He et al., 2012).

Early studies using SHG microscopy to image biological tissue involved examining type I collagen in rat tail tendon (Freund et al., 1986; Roth & Freund, 1981). Since ultrafast pulse laser technology did not exist at the time, techniques were limited to a large focal spot size using a nanosecond laser, which produced low resolution images (Stoller et al., 2002). With the introduction of short-pulse femtosecond titanium sapphire lasers, Stoller et al. (2002) could image type I collagen in rat tail tendon within a small focal spot. This sped up the imaging process as well as produced high resolution images of collagen structure. The use of an ultrafast pulse laser further allowed for polarization dependent SHG signals to be analyzed by rotating polarized light at different angles (Stoller et al., 2002).

1.6 Second Harmonic Generation-based Quantification of Collagen Structure

Previous studies have used SHG light intensity as a parameter to quantify collagen organization in the extracellular matrix (Cox et al., 2003; Hase et al., 2016; Pendleton et al., 2020; Sugita et al., 2021; Zoumi et al., 2002). The degree of SHG light intensity within an image can provide information such as the density and the general alignment of collagen fibers (Ogura et al., 2019). However, brightness-based image analysis is not an ideal technique to quantify collagen organization because SHG light intensity is affected by other confounding factors (Ogura et al., 2019). Such factors include optical scattering, thickness of tissue samples, and the intensity of the incident laser beam (Ogura et al., 2019). Furthermore, an increase in SHG image brightness may simply be caused by collagen aggregation within a small region of the tissue

sample, which is not necessarily indicative of collagen disorganization in cancer progression (Gole et al., 2020).

One method to further analyze SHG intensity images is by conducting texture analysis. Texture analysis involves defining regions of the intensity image based on texture content (Ogura et al., 2019). Quantitative characterization based on textural qualities such as density and directionality of collagen is carried out by using spatial variation in pixel intensities as a function (Fung et al., 2010; Ogura et al., 2019; Rentchler et al., 2019). However, texture analysis is restricted to a large region size, meaning that it is restricted to analyzing collagen organization at a cellular scale, rather than its ultrastructure (Ambekar et al., 2012; Tokarz et al., 2020).

Polarization-sensitive SHG (PSHG) analysis is an alternative method over texture analysis to quantify collagen organization from an SHG intensity image (Stoller et al., 2002; Tokarz et al., 2020; Williams et al., 2005). PSHG analysis involves recording SHG images at varying angles of the input laser polarization (Ambekar et al., 2012; Chen et al., 2012; Hristu et al., 2022; Tokarz et al., 2020). This allows polarization-sensitive SHG parameters to be obtained, which quantify the ultrastructural organization of collagen in the ECM in a small, single laser focal volume (Chen et al., 2012; Golaraei et al., 2020; Hristu et al., 2022; Tokarz et al., 2020). Previous studies using PSHG have demonstrated that there was a significant difference in collagen ultrastructure between normal and pathological human tissue samples, such as in the breast, thyroid, lung, and pancreas (Ambekar et al., 2012; Golaraei et al., 2016, 2020; Tokarz et al., 2019, 2020). These studies observed that collagen structure is more disorganized in a malignant tumour microenvironment compared to that observed in the ECM in normal tissue.

1.7 Objectives

The main goal of the study is to use a quantitative approach to compare normal and pathological stomach tissue with varying levels of adenocarcinoma differentiation using polarization-sensitive SHG microscopy (PSHG). This addresses the current limitations in gastric cancer diagnosis where pathologists rely on morphological interpretations of H&E-stained specimen that may result in an inaccurate and untimely diagnosis. Observing quantifiable changes in collagen ultrastructure in the ECM for the different conditions of stomach tissue can allow the evaluation of gastric adenocarcinomas to be standardized across institutions. Provided we can observe quantifiable changes in collagen structure, PSHG can potentially serve as a complementary tool for pathologists in addition to traditional diagnostic methods.

Reaching the study goal will involve three objectives:

The first objective of the study is to obtain SHG light intensity images from gastric cancer and normal stomach tissue samples using SHG microscopy. My approach to meet this objective was by imaging tissue samples that were already sectioned and fixed on microscope slides from a patient group. SHG signals emitted from collagen ultrastructure in the extracellular matrix will allow for visualization of the tissue samples through the form of an intensity image. This objective ensures that enough SHG signal is emitted from each sample region. Since the study takes the approach of analyzing collagen ultrastructure as a potential cancer biomarker, it is essential that there is enough collagen present in the ECM of tissue regions that can later be analyzed. This can be achieved by evaluating the brightness of the pixels in the intensity images with an intensity bar that assigns a pixel to a brightness value, where relative brightness indicates the strength of the emitted SHG signal.

The second objective of the study is to obtain PSHG parameters from each scan performed for the different tissue samples. This requires collecting images with polarization-in, polarization-out (PIPO) SHG microscopy. The PIPO SHG technique involves taking 64 SHG intensity images at different linear polarization angles of the incident laser (Cisek et al., 2021). As a result, a stacked image containing the 64 images can be obtained. The stacked image can then be fitted using a program that assigns a relationship between SHG intensity and the linear polarization orientation of the laser at different angles (Cisek et al., 2021; Tokarz et al., 2019, 2020). This allows us to extract PSHG parameters from the fitted images that can be used for quantitative analysis.

The third objective is to analyze PSHG parameters to compare normal and pathological stomach tissue. It is expected that collagen in normal stomach tissue will have a higher degree of structural order compared to pathological samples, as observed in previous PSHG studies examining breast, thyroid, lung, and pancreas tissue (Ambekar et al., 2012; Golaraei et al., 2016, 2020; Tokarz et al., 2019, 2020). It is also expected that as the cancerous tissue condition progresses from well differentiated to poorly differentiated adenocarcinoma, the collagen ultrastructure becomes more disorganized. The reasoning behind this hypothesis is that tumours become more aggressive as they progress from a high to low level of differentiation, marked by a decline in survival rate (Adachi et al., 2000; Jögi et al., 2012). Consequently, a greater degree of dysregulated collagen remodelling in the microenvironment for poorly differentiated adenocarcinomas is expected.

2. Materials and Methods

2.1 Microscope Slide Preparation

The following protocol for microscope slide preparation was performed by SuperBioChips Laboratories (Cancer Research Institute Seoul National University). Biopsies were obtained from pathological tissue regions of the stomach from fifty-nine patients. Of those same patients, biopsies were also obtained from non-cancerous tissue regions from the stomach. Tissue samples were fixed with formalin and then dehydrated with 70%, 90%, 95%, 99% and 100% ethanol for one hour at each progressive step. The tissues were cleared by xylene for an hour. They were immersed in paraffin at 60 °C for an hour. The fixation, dehydration, clearing and immersion steps were repeated for a total of three times. Using a microtome, the tissues were sectioned into circular cores measuring 2 mm (2000 μm) in diameter and 4 μm in thickness. For second harmonic generation (SHG) imaging, thin sections of tissue (< 5 μm) are required to minimize the optical effects of birefringence, since thicker sections result in changes to the polarization state of the incident laser beam. The cores were placed on a New Silane III Slide from Muto Pure Chemicals Co.

One microscope slide containing fifty-nine tissue cores of pathological human stomach tissue (CQ2) and one slide with fifty-nine tissue cores of normal stomach tissue (CQN2) from matching patients were obtained from SuperBioChips (Figure 3). Tissue core samples were obtained from male and female patients ranging from 40-72 years old. The conditions for pathological tissue samples included the following: poorly differentiated adenocarcinoma, moderately differentiated adenocarcinoma, well differentiated adenocarcinoma, signet ring cell carcinoma, mucinous adenocarcinoma, and undifferentiated carcinoma (Appendix I). However, I

only investigated normal tissue, poorly differentiated, moderately differentiated and well

differentiated adenocarcinoma samples for the purposes of this study (Appendices I and II). This

was due to time constraints and because the focus of the study was to characterize the varying

degrees of adenocarcinoma differentiation and to distinguish these pathological samples from

normal tissue based on SHG microscopy.
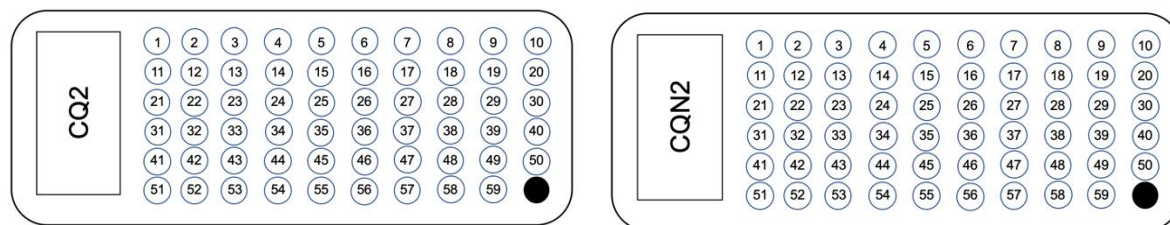
Figure 3. **Schematic diagram of microscope slides with stomach tissue biopsy samples**. CQ2 contained fixed pathological stomach tissue samples from fifty-nine patients (Appendix I). From the same patients, normal stomach tissue adjacent to the pathological tissue were also prepared as fifty-nine sample cores on the slide labelled CQN2 (Appendix II).

2.2 Polarization-in, Polarization-out Second Harmonic Generation (PIPO SHG) Microscopy

2.2.1 Landmark Identification

The following PIPO SHG microscopy protocol was performed in a Class 4 Laser

Laboratory at Saint Mary's University, Halifax, NS. I placed a coverslip (VWR Micro Cover

Glass, 18 x 18 mm) over each of the two slides prior to imaging the samples. This was to prevent

any direct abrasion of tissue samples by the objective lens when moving the slide on the stage of

the microscope. I secured the coverslips to the slides by applying a thin layer of Sally Hansen

Xtreme Wear Clear nail polish on the edges. The slides were left to dry in a temperature-controlled laboratory at 21°C for 48 hours.

To mark the location of identifiable landmark regions within each core, I performed high-resolution brightfield microscopy prior to using SHG microscopy. This is because high-resolution brightfield microscopy uses white light, which provides a macrostructural view of the entire tissue core. Each tissue core for both slides was imaged using the Olympus CH-2 Brightfield microscope with a 4X objective lens. A digital camera was connected to the brightfield microscope and to the computer, which allowed the brightfield image to be visualized through AmScope 3.7 software. The resulting brightfield image size was 2686 μm × 2149 μm (Figure 4). The brightfield image allowed for the identification of landmark regions, which were characterized by holes in the tissue sample.

For each core, I recorded landmark regions that were relative to an origin point set as the coordinates (0, 0) by using the built-in coordinate system of the SHG microscope stage (x, y coordinates). Three to four landmark regions were recorded for each brightfield image (Figure 4). This initial step of recording landmarks using brightfield microscopy and imaging the overall tissue core was crucial for the later steps of SHG imaging because the SHG image size (98 μm × 98 μm) is smaller than the brightfield image and is only specific to collagen ultrastructure.
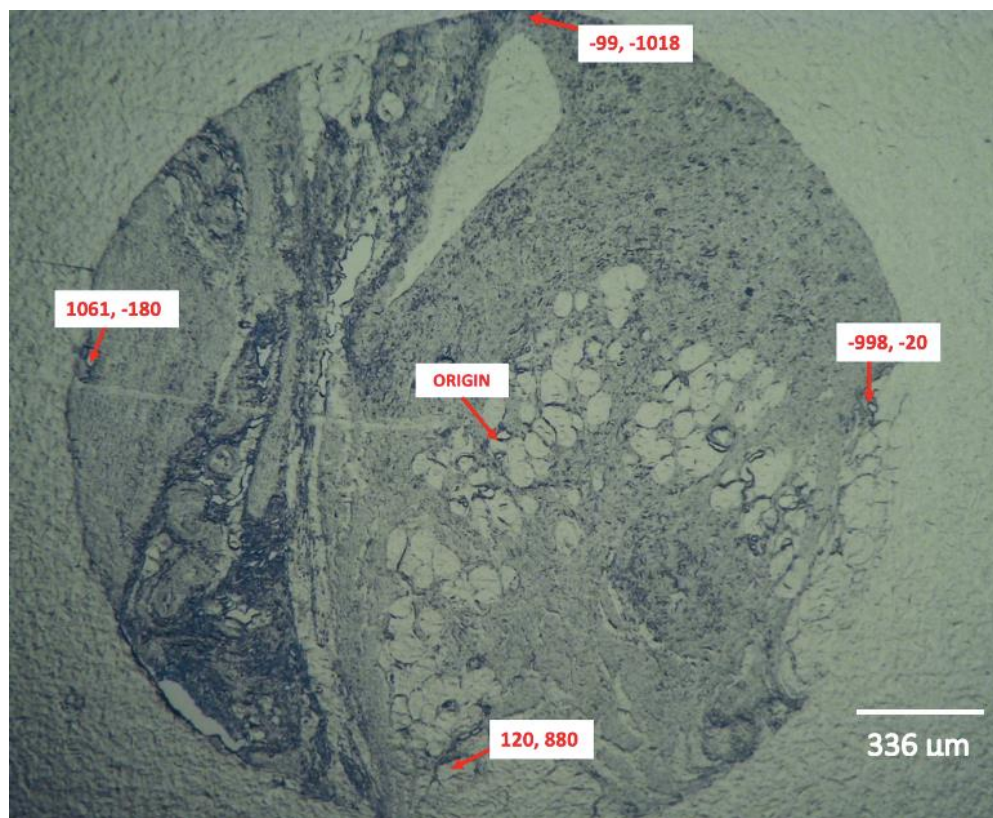
Figure 4. **High-resolution brightfield microscope image of core #40 from the CQ2 slide, from a patient with poorly differentiated adenocarcinoma.** The arrow labelled "origin" indicates the point manually set to coordinate (0, 0). Landmark regions of the core are marked by arrows labelled with a coordinate that is relative to the point of origin. A scale bar measuring 336 μm is included for reference.

2.2.2 Non-linear Optical Microscope Set-up and SHG Intensity Imaging

A custom-built non-linear optical microscope paired with a femtosecond laser as an excitation source was used to perform PSHG using the technique, polarization-in, polarization-out second harmonic generation (PIPO SHG) microscopy. Figure 5 shows how the non-linear optical microscope was set up. The femtosecond laser used was a FemtoLux 3 laser from Ekspla, operating at 1030 nm in wavelength. 250 femtosecond (fs) pulses were repeated by the laser at a rate of 5 megahertz (MHz). With a 0.8 numerical aperture Plan-Apochromat 20× excitation objective (EO) lens from Carl Zeiss AG, the laser beam was focused on the sample region on the microscope slide (Figure 5).

The laser beam was raster scanned across the region chosen for imaging from each sample by using a pair of ScannerMAX galvanometric scan mirrors from Pangolin Laser Systems Inc (Figure 5). The process of raster scanning involves the laser beam moving across the selected region, one row at a time, from top to bottom, in a zig zag pattern. The average laser beam power used to image samples on the two microscope slides was 1.9 mW.

SHG signals were collected for each scan by using a collection objective lens (CO) that was integrated into the custom-built non-linear optical microscope (Figure 5). The collection objective lens was a 0.85 numerical aperture lens from Omex Technologies. A 65-153 Edmund Optics interference filter (F) was also used to collect SHG signals at 515 nm at a bandwidth of 10 nm (Figure 5). To measure the SHG signals that were collected, a photomultiplier tube (PMT) was integrated into the non-linear optical microscope, which recorded the number of photons detected in the SHG scan (Figure 5).

SHG intensity images each containing 100×100 pixels with an image size of 98×98 μm were collected. SHG intensity images were uploaded onto the ImageJ image-processing program developed by the National Institutes of Health. I inspected each image by observing that there was enough SHG intensity prior to proceeding with PIPO SHG imaging and analysis, which indicated that there was sufficient collagen present in the sample to be analyzed. This was done by observing the intensity value associated with the brightest pixel present in the SHG intensity image. I performed the following PIPO SHG imaging procedure for SHG intensity images containing a pixel with an intensity value greater than 300.

2.2.3 PIPO SHG Imaging

Polarization-sensitive SHG images were obtained based on the PIPO SHG technique by
Tuer et al. (2011). A polarization-state generator (PSG) which consisted of a stationary linear
polarizer (LPVIS100 from Thorlabs) and a motorized rotating half-wave plate (WPMP2-22-
V1030 from Karl Lambrecht Corp.) was placed before the EO lens in the non-linear optical
microscope (Figure 5). The PSG set-up in the microscope allowed the incident laser linear
polarization to be rotated. To measure the linear polarization angle of the SHG signal, a
polarization state analyzer (PSA) was incorporated in the microscope by placing it after the CO
lens (Figure 5). The PSA consisted of a polarizing filter (LPVISA 100 from Thorlabs) placed on
a motorized rotating mount.
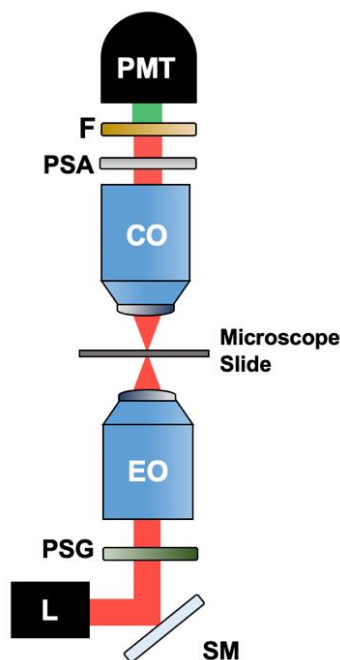
Figure 5. **Simplified diagram of the non-linear optical microscope set-up for PIPO SHG imaging.**
The source of the incident laser beam comes from the laser (L), which raster scans the tissue sample by
the scanning mirrors (SM). The polarization state generator (PSG) was placed before the excitation
objective lens (EO), which focuses the laser beam onto the tissue sample. The microscope slide
containing tissue core samples was placed on a motorized stage. The collection objective lens (CO) was
placed after the microscope slide and before the polarization state analyzer (PSA). The interference filter
(F) was placed before the photomultiplier tube (PMT) to collect SHG signals.

A PIPO SHG scan included 65 SHG images obtained by first using 8 linear polarization angles of the PSA for each of the 8 PSG half-wave plate angles, followed by an additional scan at the initial PSA and PSG settings. 100 frames were taken for each of the 65 SHG images. The resulting PIPO image size was 98 × 98 μm, with an image resolution of 100 × 100 pixels. I performed four PIPO SHG scans of different regions for each core from both the normal and pathological stomach tissue slides (Appendices I and II). I did not perform PIPO SHG scans of sample cores that did not produce sufficient SHG signals, as noted in Appendices I and II. Each PIPO SHG scan took approximately 20 minutes to perform. When not scanning, I stored the microscope slides in a refrigerator at 4°C to preserve the tissue samples.

The image quality of the PIPO SHG scans were verified by using the ImageJ program to compare the SHG intensity profiles of the pixels between the first image and last image acquired from the PIPO SHG scan. Prior to PIPO SHG analysis, I ensured that the SHG intensity profiles of the first image and the last image in the stack of 65 images were identical. If the first and last images were not identical, the PIPO SHG scan was not included as a part of the analysis, and another scan was performed as a substitute. This step ensured that there was no sample movement and that there was no photodamage to the samples, which could have altered the intensity of the SHG signals during the scanning process.

2.3 Polarization-in, Polarization-out Second Harmonic Generation (PIPO SHG) Analysis

The following procedure for PIPO SHG analysis was adapted from Tuer et al. (2011). Analysis of data was performed by assuming that collagen fibers in tissue sections possess cylindrical hexagonal (C_{6v}) symmetry, with a vertical mirror plane. Using the laboratory

Cartesian coordinate system (XYZ), the direction of the laser beam of the non-linear optical microscope was defined along the Y axis (Figure 6). The laboratory coordinate system also defines the image plane at XZ (Figure 6). Figure 6 also shows an arbitrarily oriented collagen fiber present in the ECM of a tissue sample. The collagen fiber is oriented so that it projects off of the XZ image plane. δ represents the in-plane collagen fiber orientation measured from the Z-axis, while α represents the out-of-plane tilt angle of the fiber (Figure 6).
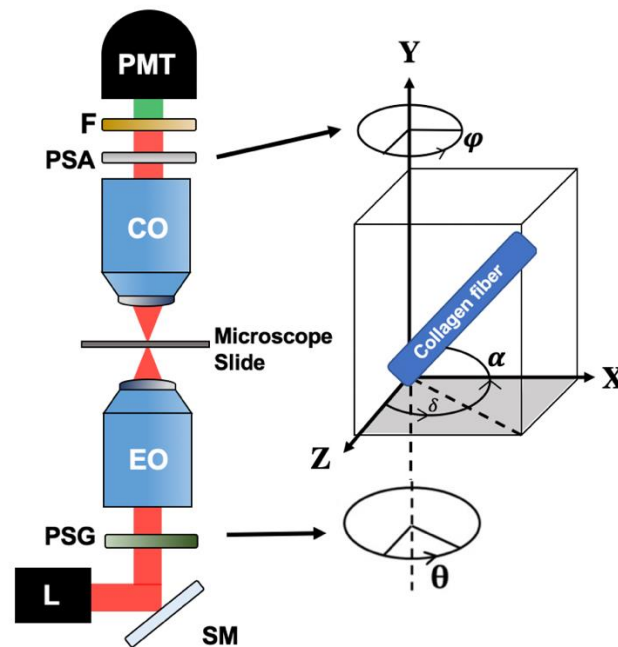
Figure 6. **Laboratory coordinate system of the non-linear optical microscope set-up used for PIPO SHG analysis.** The laboratory coordinate system (XYZ) defines the image plane (XZ), shaded in light grey, and defines the propagation direction of the laser beam along the Y-axis. An arbitrarily oriented collagen fiber that projects off the image plane is represented as a thick blue rectangle.

Equation (1) represents the SHG intensity ($I_{2\omega}$) as a function of the laser electric field polarization orientation (θ) and the PSA orientation (φ). θ and φ are also labelled in Fig. 6 to demonstrate their relationship to the laboratory coordinate system.

$$I_{2\omega} \propto \left| \begin{array}{c} \sin(\varphi - \delta) \sin 2(\theta - \delta) + \cos(\varphi - \delta) \sin^2(\theta - \delta) + \\ \boldsymbol{\rho} \cos(\varphi - \delta) \cos^2(\theta - \delta) \end{array} \right|^2 \quad (1)$$

The PIPO SHG parameter used to compare collagen ultrastructure between pathological and normal tissue in this study was ρ, which is a second-order non-linear optical susceptibility tensor component ratio that can be derived from Equation (1). I obtained the ρ parameter value for each pixel within each PIPO SHG scan. The ρ value is related to the degree of variations in the helical pitch angle of a cylindrical collagen molecule (Tiaho et al., 2007). Helical pitch is the distance between two points on a helix that are one turn apart from each other, relative to a central axis (Figure 7). The helical pitch angle is the angle between the helix twist and the central axis (Figure 7).
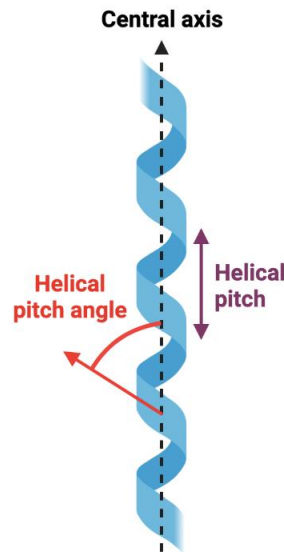
Figure 7. **Proposed geometric structure of a single collagen helix by Tiaho et al. (2007).** The central axis, represented by a vertical hashed line, orients the collagen helix in three-dimensional space. Helical pitch (in purple) is the distance between two points of the helix that are one turn apart. Helical pitch angle (in red) is measured from the central axis to the point of a cylindrical helix twist. The schematic diagram was created on BioRender.

Since ρ is related to the variations in pitch angles of the triple helices in a collagen

molecule, we can use this parameter to quantify the degree of disorder in collagen at an

ultrastructural, molecular level. Biological tissue regions that have a ρ value of closer to 3

represent a greater degree of ultrastructural disorder in collagen (Simpson & Rowlen, 1999). In

contrast, tissue regions with ρ values of less than 3 are associated with lower degrees of

structural disorder in collagen (Simpson & Rowlen, 1999). Therefore, a greater ρ value for

stomach tissue regions was associated with a higher degree of structural disorder in collagen for

the purposes of this study (Brittain et al., 2022; Cisek et al., 2021; Tokarz et al., 2019, 2020).

Using a custom MATLAB program, each PIPO SHG scan was fitted with Equation (1) to

obtain the ρ values associated with each pixel in the scan. To ensure quality of fitted data, only

PIPO SHG scans with a goodness of fit (R^2) greater than 0.8 were considered for analysis

(Appendices I and II). Furthermore, only PIPO SHG images with a number of fitted pixels

greater than 700 within the image were considered for analysis (Appendices I and II). The mean

ρ value was then recorded for each PIPO SHG scan by fitting an occurrence histogram of the ρ

values with a Gaussian function and obtaining the centre position of the Gaussian function in the

MATLAB program.

2.4 Statistical Analysis

Since a matching core number on the stomach tissue slides indicated that the normal and

the pathological tissue were sectioned from the same patient, it was appropriate to perform a

paired-sample t-test. The mean ρ value was treated as the dependent variable. I performed this

test to determine if there was a significant difference in the mean degree of collagen structural

disorder (ρ) between pathological stomach tissue in patients and their matching normal tissue. A statistical P value of less than 0.05 was deemed statistically significant. To further determine if there was a specific type of adenocarcinoma that was representative of patient cases for differences in the mean degree of collagen structural disorder (ρ), I conducted separate paired-sample t-tests. Three additional paired-sample t-tests were conducted for patients who were diagnosed with well differentiated, moderately differentiated, and poorly differentiated gastric adenocarcinomas to determine if there was a significant difference in the mean degree of collagen structural disorder (ρ) compared to their matching normal tissue samples. A statistical P value of less than 0.05 was considered significant.

In addition to using patients as the sample size for statistical analysis, I also used the number of PIPO SHG scans belonging to each stomach tissue type as the sample size. I conducted six independent samples two-tailed t-tests to test for a significant difference in mean ρ values of PIPO SHG scans between two tissue groups at a time. The mean ρ value of the PIPO SHG scans was treated as the dependent variable. The independent variable was the stomach tissue type, which included the following: normal tissue, well differentiated, moderately differentiated, and poorly differentiated gastric adenocarcinomas. A statistical P value of less than 0.05 was deemed significant.

Statistical analyses were performed in Microsoft Excel and RStudio.

3. Results

3.1 Polarization-in, Polarization-out Second Harmonic Generation (PIPO SHG) Scans and Fitted ρ Values

PIPO SHG scans were performed according to the procedures in section 2.2 to determine if collagen can be successfully imaged from stomach tissue samples and if ρ values can be extracted from the scans. The top row in Figure 8 shows SHG intensity images of PIPO SHG scans performed on typical sample regions from normal, well differentiated (WDA), moderately differentiated (MDA) and poorly differentiated (PDA) gastric adenocarcinoma tissues. Each SHG intensity image (A1-D1) is 98 µm × 98 µm big. Each SHG intensity image has an image resolution of 100 × 100 pixels. The white striations within the images (A1-D1) are a visualization of collagen in the ECM. This visualization is possible since collagen molecules emit SHG signals that are captured by the collection filter and detector from the non-linear optical microscope. The brighter pixels indicate a greater SHG intensity value, as represented by the gray-scale intensity bar in Figure 8.

The second row in Figure 8 shows colour-coded maps (A2-D2) of the fitted ρ values from collagen visualized from their matching SHG intensity images in the first row (A1-D1). Each pixel in the colour-coded map is associated with a ρ value, as indicated by the colour legend. The red pixels indicated a greater ρ value, up to a maximum value of 4.0 (as indicated by dark red pixels). The blue pixels indicated a lower ρ value, down to a minimum value of 1.0 (as indicated by dark blue pixels). Greater ρ values were associated with a greater degree of structural disorder in collagen.
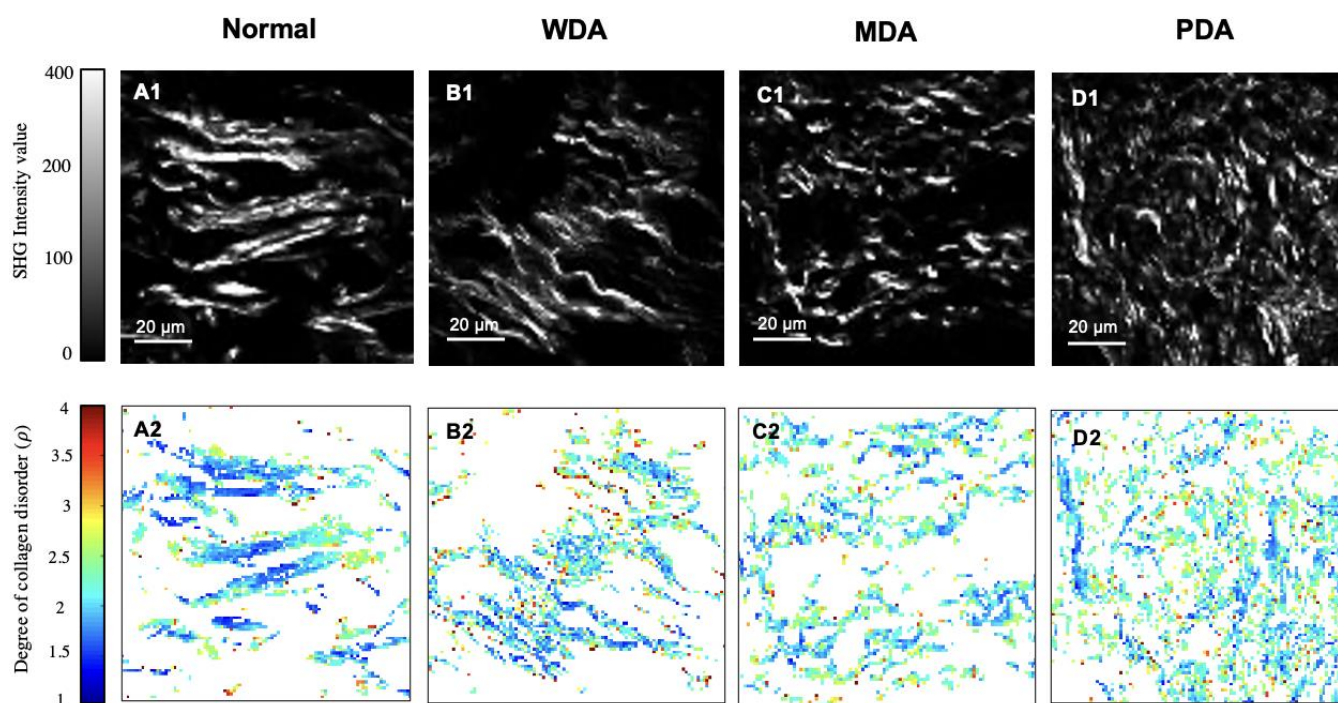
Figure 8. **Typical intensity images of polarization-sensitive second harmonic generation (PSHG) scans performed on pathological stomach tissues and their corresponding colour-coded maps of ρ values.** The intensity images and colour-coded maps represent typical sample regions from the following stomach tissue types from left to right (A-D): normal tissue, WDA (well differentiated adenocarcinoma), MDA (moderately differentiated adenocarcinoma, and PDA (poorly differentiated adenocarcinoma). Images along the first row (A1-D1) represent intensity images of polarization-sensitive SHG scans performed for the stomach tissue types. The gray-scale intensity bar represents the associated SHG intensity value for pixels within each image. Each scale bar represents 20 μm. Colour-coded maps along the second row (A2-D2) represents collagen structure associated with a degree of disorder (ρ) for each stomach tissue type. This was obtained after each pixel from the PSHG scan (A1-D1) was fitted to obtain a ρ value. Each pixel within maps A2-D2 represents a specific ρ value according to the colour legend, which encompasses ρ values with a range from 1.0-4.0.

As shown in Figure 8, the results of the SHG intensity images demonstrated that collagen can be successfully imaged and visualized by the SHG microscopy technique. However, it was difficult to determine the distribution of ρ values among different stomach tissue groups by looking at the colour-coded map images alone in Fig. 8. Therefore, the standardized approach to analyze ρ values within each colour-coded map was to count the number of pixels that were associated with a specific ρ value. Figures 9-12 respectively show typical occurrence histograms for sample regions in normal, well differentiated, moderately differentiated, and poorly differentiated adenocarcinoma tissue types. Figures 9-12 show that the points of the occurrence histograms were fit with a Gaussian function, and the centre position of the function was used to obtain a ρ value. The purpose of the fitting of Gaussian functions for the occurrence histograms was to obtain a mean ρ value ($\pm$ standard deviation) that was representative of the degree of collagen disorder within the sample region.

Figure 9 shows that the representative ρ value for the PIPO SHG scan performed on a normal tissue sample region (Column A, Fig. 8) was 1.98 ($\pm$ 0.03). Figure 10 shows that the representative mean ρ value for the PIPO SHG scan performed for a well differentiated adenocarcinoma tissue sample region (Column B, Fig. 8) was 2.04 ($\pm$ 0.03). In Figure 11, the representative mean ρ value for the PIPO SHG scan performed for a moderately differentiated adenocarcinoma tissue sample region (Column C, Fig. 8) was 2.14 ($\pm$ 0.02). Figure 12 shows that the representative ρ value for a poorly differentiated adenocarcinoma tissue sample region (Column D, Fig. 8) was 2.16 ($\pm$ 0.02).
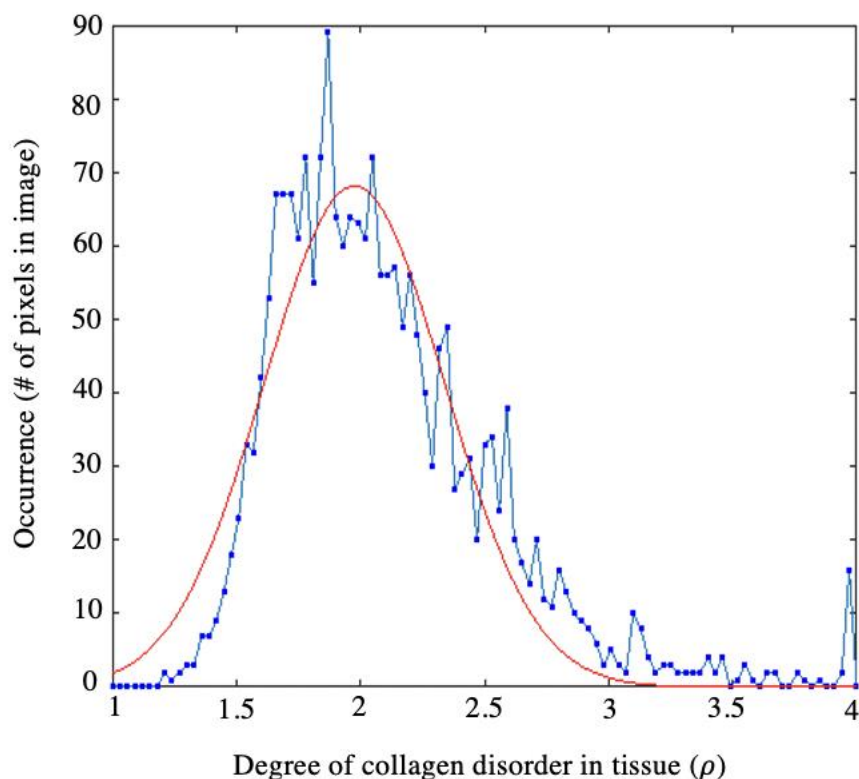
Figure 9. **Occurrence histogram of fitted ρ values from a typical sample region in a normal tissue type, corresponding with the colour-coded map (A2) in Figure 8.** The x-axis represents the degree of collagen disorder (ρ) in the normal tissue region that was scanned with PIPO SHG microscopy. The y-axis represents the occurrence, which was measured by counting the number of pixels present within the colour-coded map that was associated with a specific ρ value. The points on the graph were fit with a Gaussian function (in red), and the centre position of the function was obtained. The centre position resulted in a mean ρ value of 1.98 ($\pm$ 0.03).
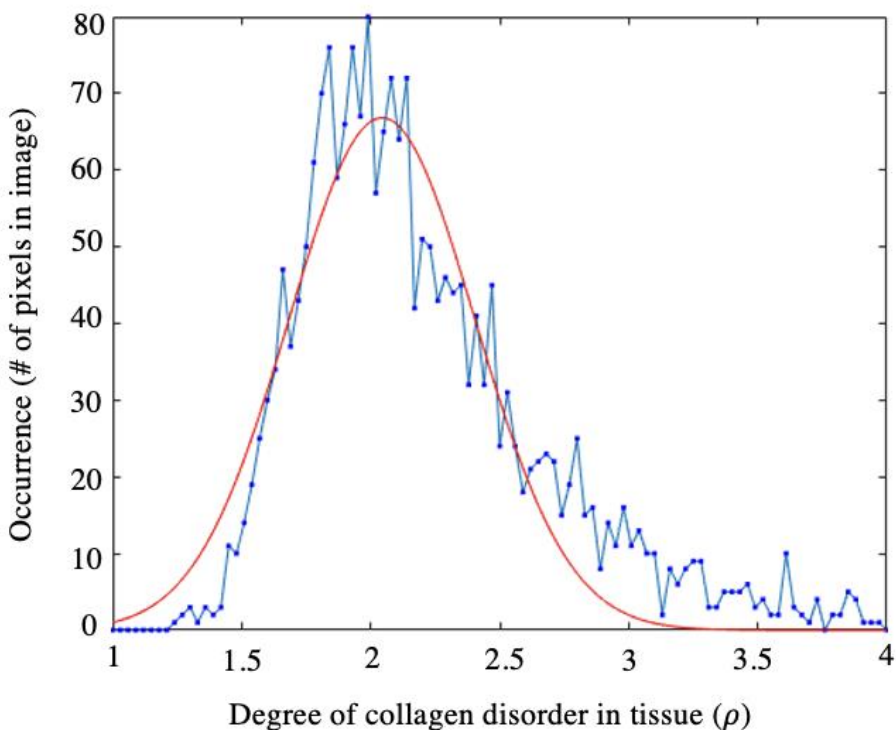
Figure 10. **Occurrence histogram of fitted ρ values from a typical sample region in a well differentiated adenocarcinoma tissue type, corresponding with the colour-coded map (B2) in Figure 8.** The x-axis represents the degree of collagen disorder (ρ) in the normal tissue region that was scanned with PIPO SHG microscopy. The y-axis represents the occurrence, which was measured by counting the number of pixels present within the colour-coded map that was associated with a specific ρ value. The points on the graph were fit with a Gaussian function (in red), and the centre position of the function was obtained. The centre position resulted in a mean ρ value of 2.04 ($\pm$ 0.03).
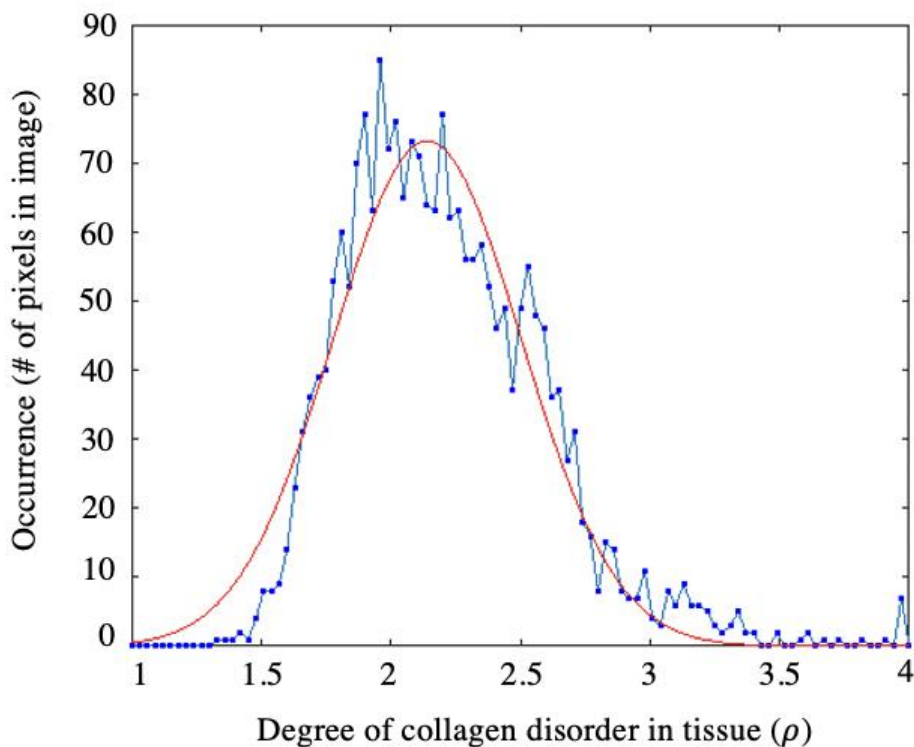
Figure 11. **Occurrence histogram of fitted ρ values from a typical sample region in a moderately differentiated adenocarcinoma tissue type, corresponding with the colour-coded map (C2) in Figure 8.** The x-axis represents the degree of collagen disorder (ρ) in the normal tissue region that was scanned with PIPO SHG microscopy. The y-axis represents the occurrence, which was measured by counting the number of pixels present within the colour-coded map that was associated with a specific ρ value. The points on the graph were fit with a Gaussian function (in red), and the centre position of the function was obtained. The centre position resulted in a mean ρ value of 2.14 (± 0.02).
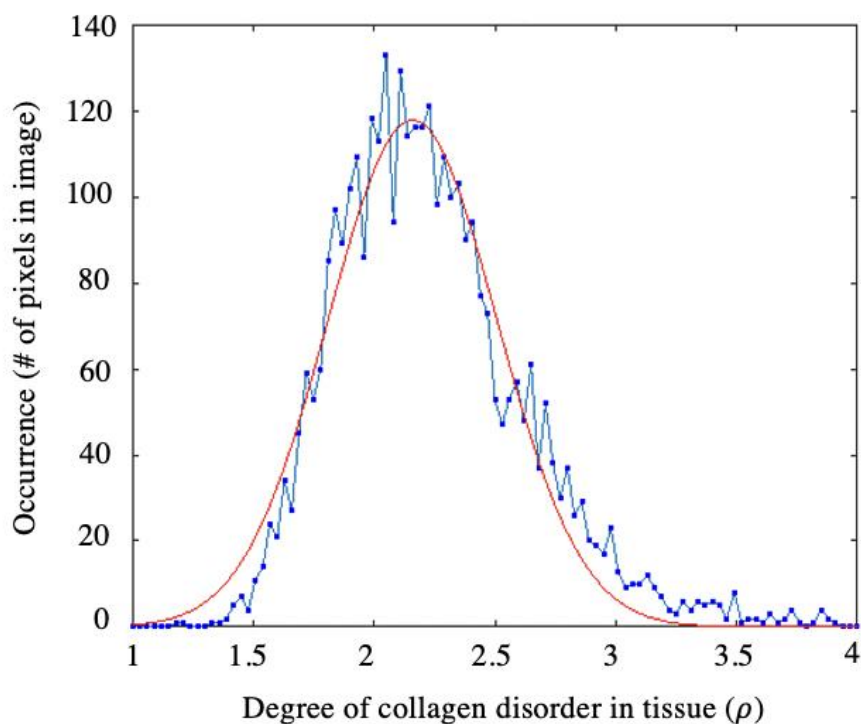
Figure 12. **Occurrence histogram of fitted ρ values from a typical sample region in a poorly differentiated adenocarcinoma tissue type, corresponding with the colour-coded map (D2) in Figure 8.** The x-axis represents the degree of collagen disorder (ρ) in the normal tissue region that was scanned with PIPO SHG microscopy. The y-axis represents the occurrence, which was measured by counting the number of pixels present within the colour-coded map that was associated with a specific ρ value. The points on the graph were fit with a Gaussian function (in red), and the centre position of the function was obtained. The centre position resulted in a mean ρ value of 2.16 ($\pm$ 0.02).

3.2 Comparison of Collagen Disorder between Pathological and Normal tissues in Matching Patients

A paired-sample t-test was performed to determine if there was a significant difference in the mean degree of collagen structural disorder ($\rho$) between pathological stomach tissue in patients and their matching normal tissue. There was a significantly greater mean degree of collagen structural disorder (ρ) for pathological stomach tissue samples in patients compared to their matching normal tissue, as P = 0.04 (Table 1). Therefore, the null hypothesis (H_0) that there is no significant difference in the mean degree of collagen structural disorder between cancerous and normal tissues in patients was rejected. Figure 13 further demonstrates that there was a higher proportion of cases where the degree of collagen disorder increased from normal stomach tissue to their matching pathological tissue type (well differentiated, moderately differentiated, and poorly differentiated adenocarcinomas). There was an increase in collagen structural disorder for the cancerous stomach tissue group for 66% of patients (Fig. 13).

Table 1. Paired-sample t-test statistics performed to test for a significant difference in the mean degree of collagen structural disorder (ρ) between pathological stomach tissue in patients and their matching normal tissue. Data for collagen disorder are presented as mean $\pm$ standard deviation. A P value of less than α (0.05) was considered statistically significant.

Stomach tissue group, *n* patients	Collagen disorder (ρ)	*t* value (two-tailed)	P value
Cancer, 32	2.10 ± 0.01	2.111	0.0430
Normal, 32	2.05 ± 0.01		
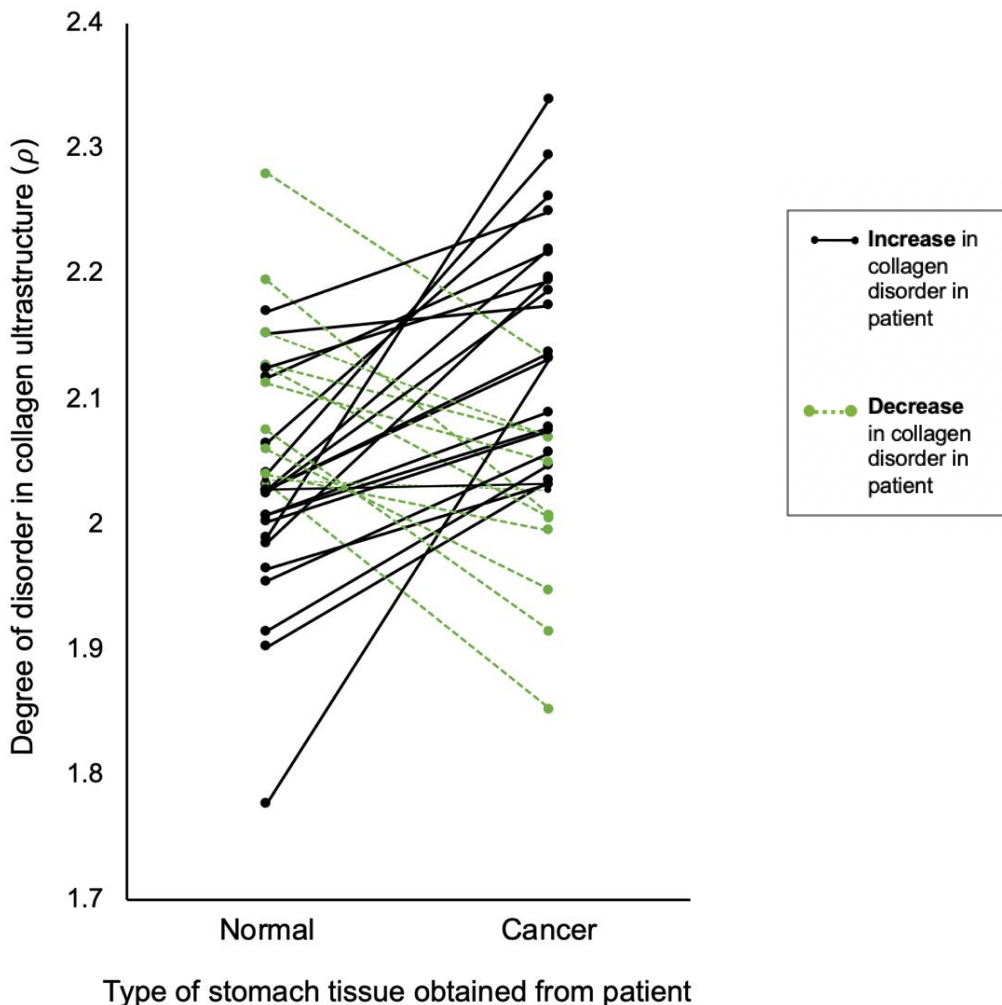
Figure 13. **Differences in degree of collagen disorder (ρ) between cancerous tissue and the adjacent normal tissue from patient.** The x-axis represents the type of stomach tissue obtained from each patient (n = 32 patients). The cancerous tissue group included well differentiated (n = 5 patients), moderately differentiated (n = 7 patients), and poorly differentiated (n = 20 patients) gastric adenocarcinomas. The y-axis represents the degree of disorder in collagen structure (ρ). The ρ value points obtained from each patient for their cancerous tissue and matching normal tissue samples are connected by a line to demonstrate either an increase (black solid line) or a decrease (green hashed line) in collagen disorder.

To further determine if there was a specific type of adenocarcinoma that was representative of the cases where collagen disorder increased from normal to pathological stomach tissue, separate paired-sample t-tests were conducted for patients who were diagnosed with well differentiated, moderately differentiated, and poorly differentiated gastric adenocarcinomas. There was no significant difference in the mean degree of collagen disorder (ρ) for tissues affected by well differentiated gastric adenocarcinoma compared to their matching normal tissue in patients, $t(4) = -0.74$, P = 0.50 (Table 2). Likewise, there was no significant difference in the mean degree of collagen structural disorder (ρ) for tissues affected by moderately differentiated gastric adenocarcinoma compared to their matching normal tissue, $t(6) = 2.09$, P = 0.08 (Table 3). There was no significant difference in the mean degree of collagen structural disorder (ρ) for tissues affected by poorly differentiated gastric adenocarcinoma compared to their matching normal tissue in patients, $t(19) = 1.62$, P = 0.12 (Table 4). The results of the paired-sample t-tests (Tables 2-4) suggest that another approach for statistical testing should be taken when comparing collagen structures across different gastric adenocarcinoma groups. This rationale was also attributed to a small sample size for the number of patients that could be used in the paired-sample t-tests for each type of gastric adenocarcinoma tissue (Tables 2-4).

Table 2. Paired-sample t-test statistics performed to test for a significant difference in the mean degree of collagen structural disorder (ρ) between well differentiated gastric adenocarcinoma (WDA) in patients and their matching normal tissue. Data for collagen disorder are presented as mean ± standard deviation. A P value of less than α (0.05) was considered statistically significant.

Stomach tissue group, *n* patients	Collagen disorder (ρ)	*t* value (two-tailed)	P value
WDA, 5	2.03 ± 0.1	-0.744	0.498
Normal, 5	2.05 ± 0.05		

Table 3. Paired-sample t-test statistics performed to test for a significant difference in the mean degree of collagen structural disorder (ρ) between moderately differentiated gastric adenocarcinoma (MDA) in patients and their matching normal tissue. Data for collagen disorder are presented as mean ± standard deviation. A P value of less than α (0.05) was considered statistically significant.

Stomach tissue group, *n* patients	Collagen disorder (ρ)	*t* value (two-tailed)	P value
MDA, 7	2.16 ± 0.1	2.086	0.082
Normal, 7	2.04 ± 0.1		

Table 4. Paired-sample t-test statistics performed to test for a significant difference in the mean degree of collagen structural disorder (ρ) between poorly differentiated gastric adenocarcinoma (PDA) in patients and their matching normal tissue. Data for collagen disorder are presented as mean ± standard deviation. A P value of less than α (0.05) was considered statistically significant.

Stomach tissue group, *n* patients	Collagen disorder (ρ)	*t* value (two-tailed)	P value
PDA, 20	2.10 ± 0.1	1.623	0.121
Normal, 20	2.05 ± 0.1		

3.3 Comparison of Collagen Disorder between Gastric Adenocarcinoma Groups

Since the paired-sample t-tests did not show a significant difference in the degree of collagen disorder across the different types of gastric adenocarcinoma, another statistical approach was investigated. The limitations in patient sample size occurred due to a limited number of tissue cores for patients particularly affected by well differentiated and moderately differentiated adenocarcinomas available on the microscope slides. This led to a limitation in the number of representative ρ values that could be obtained from PIPO SHG scans to observe changes in collagen disorder within the same patients. Therefore, it was appropriate to compare collagen disorder across different stomach tissue types by comparing the mean ρ values by the

number of PIPO SHG scans performed for each sample region, rather than by the number of

patients.
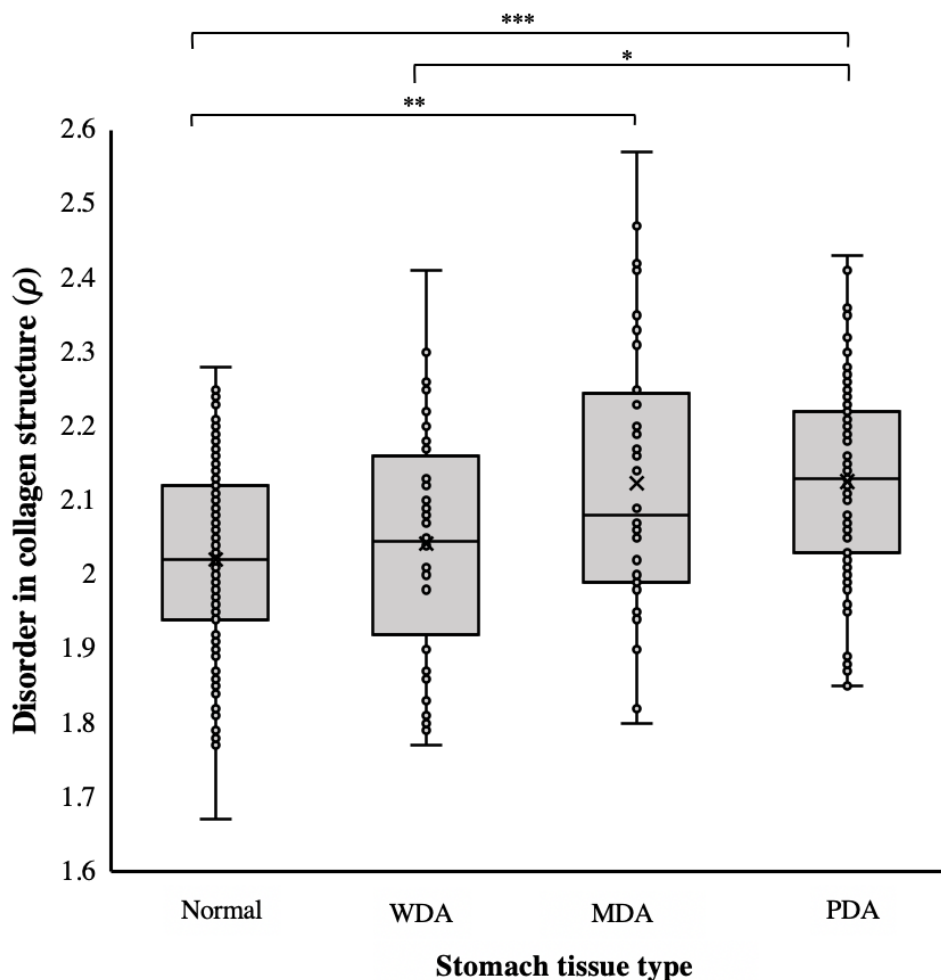
Figure 14. **Boxplots of the degree of structural disorder in collagen of normal and pathological stomach tissue types.** The x-axis represents the four different stomach tissue groups investigated in the study which included: normal, well differentiated adenocarcinoma (WDA), moderately differentiated adenocarcinoma (MDA), and poorly differentiated adenocarcinoma (PDA). The sample sizes for each group were the following: normal (n = 127 scans), WDA (n = 32 scans), MDA (n = 36 scans), and PDA (n = 83 scans). The y-axis represents the degree of disorder in collagen structure (ρ). The mean ρ values for each stomach tissue group is marked by × on the boxplot. Each point (○) on the boxplot represents the mean ρ values representative of the PIPO SHG scan performed. Six two-tailed t-tests were performed to test for a significant difference between two tissue groups. Symbol (*) denotes a P value < 0.01, symbol (**) denotes a P value < 0.001, and symbol (***) denotes a P value < 0.0001.

The boxplots in Figure 14 display data for the degree in collagen structure of PIPO SHG scanned sample regions in normal, well differentiated (WDA), moderately differentiated (MDA), and poorly differentiated (PDA) gastric adenocarcinoma tissue groups. The boxplots show a general trend in an increasing mean ρ value as the degree of adenocarcinoma differentiation becomes poorer (Fig. 14). The stomach tissue group which had the lowest minimum for the degree of collagen disorder was normal tissue, as expected (Fig. 14). The stomach tissue group with the greatest upper quartile and maximum was MDA (Fig. 14). This was unexpected because we expected to see the PDA group to have the greatest ρ value, which is associated with the greatest degree of structural disorder. However, the group with the greatest median ρ value was PDA, which was expected (Fig. 14).

Table 5. Six independent samples t-test statistics performed on RStudio to test for a significant difference in the mean degree of collagen structural disorder (ρ) between two stomach tissue groups at a time which included: well differentiated adenocarcinoma (WDA), moderately differentiated adenocarcinoma (MDA), poorly differentiated adenocarcinoma (PDA), and normal. Data for collagen disorder are presented as mean ± standard deviation. A P value of less than α (0.05) was considered statistically significant.

Stomach tissue group, n scans	Collagen disorder (ρ)	t value (two-tailed)	P value
MDA, 36 Normal, 127	2.12 ± 0.2 2.02 ± 0.1	-3.140	0.003
PDA, 83 WDA, 32	2.13 ± 0.1 2.04 ± 0.1	-2.610	0.012
PDA, 83 Normal, 127	2.13 ± 0.1 2.02 ± 0.1	-5.762	0.000
WDA, 32 Normal, 127	2.04 ± 0.1 2.02 ± 0.1	-0.717	0.477
PDA, 83 MDA, 36	2.13 ± 0.1 2.12 ± 0.2	-0.070	0.945
MDA, 36 WDA, 32	2.12 ± 0.2 2.04 ± 0.1	-1.932	0.057

Six independent samples two-tailed t-tests were performed in RStudio to test for a significant difference in mean ρ values of PIPO SHG scans between two tissue groups at a time (Table 5). Results showed that the 36 scans performed on the moderately differentiated group compared to the 127 scans performed on normal tissue had a significantly greater mean ρ value, $t(161) = -3.14$, P = 0.00 (Table 5). The significant difference between these two groups is also shown in Figure 14. Furthermore, the 83 scans performed on the poorly differentiated group compared to the 32 scans performed on well differentiated adenocarcinoma tissue had a significantly greater mean ρ value, $t(157) = -2.61$, P = 0.01 (Table 5). The greatest significant difference in mean ρ values was observed between the 83 scans performed on poorly differentiated adenocarcinoma compared to the 127 scans performed on normal tissue, $t(208) = -5.76$, P = 0.00 (Table 5). Figure 14 shows that these two groups are the furthest apart from each other in terms of their tissue morphology along the x-axis and also shows that these groups have the greatest significant difference in their means (as marked by symbol ***).

There was no significant difference in the mean ρ value between scans performed on the normal tissue and well differentiated adenocarcinoma tissue groups, $t(157) = -0.72$, P = 0.48 (Table 5). Furthermore, there was no significant differences in mean ρ values between pathological groups that were closer in terms of their degrees of tissue differentiation. For example, there was a lack of a significant difference in mean ρ values between scans performed on moderately and poorly differentiated adenocarcinomas, $t(117) = -0.07$, P = 0.95 (Table 5). There was also no significant difference between scans performed on the well differentiated tissue and moderately differentiated adenocarcinoma tissue groups, although the two-tailed P statistical value was closer to being lower than the significance level ($\alpha = 0.05$) cut-off, $t(66) = -1.93$, P = 0.06 (Table 5).

4. Discussion

In this study, I set out to determine if monitoring collagen structures in the extracellular matrix through polarization-sensitive second harmonic generation (PSHG) microscopy is an appropriate technique for characterization of pathological stomach tissue types. This involved obtaining SHG intensity images from normal tissue and gastric adenocarcinomas to visualize collagen structures. I then used the polarization-in, polarization-out (PIPO) SHG technique to obtain a mean ρ value that is representative of the collagen disorder in a stomach tissue sample region. The results demonstrated that: 1) The mean ρ value for gastric adenocarcinomas was significantly greater than that of normal tissues obtained from matching patients; 2) The mean ρ value for poorly differentiated gastric adenocarcinoma was significantly greater than that of well differentiated adenocarcinoma; 3) There were no significant differences in mean ρ values between pathological stomach tissue groups that were close in their levels of tissue differentiation.

4.1 Comparison of Collagen Disorder between Pathological and Normal Tissue

A paired-sample t-test was performed with the objective of comparing collagen disorder between pathological and normal tissues in matching patients. The significantly greater mean ρ value for the pathological tissue group indicated that there is a greater degree of collagen disorder in a tumour microenvironment compared to the adjacent normal tissue microenvironment in an individual. This result was expected, as past PSHG studies also observed significantly greater ρ values for cancerous tissue samples compared to normal tissue in the breast, thyroid, and pancreas (Golaraei et al., 2016; Tokarz et al., 2019, 2020). The increase

in ρ for cancerous tissues has been attributed to disorderly changes in the arrangement and helical pitch angles of collagen fibers in PSHG microscopy (Golaraei et al., 2014).

I also expected greater ρ values for pathological stomach tissue because homeostasis of the extracellular matrix is disturbed in a tumour microenvironment (Elgundi et al., 2019). This can be attributed to over-expression of lysyl oxidase (LOX) enzymes (Elgundi et al., 2019; Nadiarnykh et al., 2010; Xiao & Ge, 2012). Aberrant expression of LOXs can lead to disorder in collagen arrangement in the extracellular matrix and an increased collagen density (Barker et al., 2012; Xiao & Ge, 2012). Aberrant expression of LOXs can further disturb the orientation and arrangement of collagen fibers in the interstitial matrix (Peng et al., 2009). This corresponds to the disorderly changes we observed in the organization of collagen from normal to pathological stomach tissue, as measured by the ρ structural parameter.

After observing a significant increase in collagen disorder from the normal tissue group to the pathological tissue group, my study approach was to determine if there was a specific type of gastric adenocarcinoma that was representative of the increase in ρ values. When observing mean ρ values between specific gastric adenocarcinomas and their matching normal tissue samples, I did not note any significant difference using a paired-sample t-test (Tables 2-4). A possible reason for the lack of significant differences in collagen disorder was the limitation in sample size, since there were less than ten patients examined for both the well differentiated and moderately differentiated groups (Tables 2-3). Therefore, I compared collagen disorder across different stomach tissue types by the number of PIPO SHG scans performed, rather than by the number of patients.

PIPO SHG scans performed on moderately differentiated and poorly differentiated adenocarcinoma groups could be distinguished from scans performed on normal tissue. This was

because these pathological stomach groups had a significantly greater ρ value than the normal

tissue group (Fig. 14). This finding suggests that collagen structures in moderately differentiated

and poorly differentiated tumour microenvironments are more disorganized than collagen

structure in normal tissue. Furthermore, there was a greater significant difference in collagen

disorder (ρ) between the poorly differentiated adenocarcinoma group and normal tissue group

(Fig. 14). However, we could not distinguish well differentiated adenocarcinoma from normal

tissue, as there was no significant difference in mean ρ values between the two groups (Fig. 14).

These results suggest that samples obtained from poorly differentiated adenocarcinoma tissue

types is characterized more accurately compared to other adenocarcinoma groups. The

implication of these results is that patients with tissue regions affected by poorly differentiated

adenocarcinoma are ideal candidates for initial discrimination between pathological tissue and

normal tissue.

4.2 Comparison of Collagen Disorder between Gastric Adenocarcinoma Groups

Another objective of the study was to determine if PSHG microscopy can further be used

to distinguish the gastric adenocarcinoma groups that varied in their levels of tissue

differentiation. The degree of collagen disorder (ρ) for poorly differentiated adenocarcinoma was

significantly greater than that of well differentiated adenocarcinoma (Fig. 14). This matched my

prediction that collagen structure becomes more disorganized as cancer progresses from well

differentiated to poorly differentiated. The greater degree of disorder in collagen ultrastructure

for poorly differentiated stomach tissue also corresponds to previous studies that observed a

haphazard, random arrangement of collagen fibers in poorly differentiated oral squamous cell

carcinomas (Bordoloi et al., 2020). This observation further suggests that disordered collagen structures is linked to tumour aggression, since poorer levels of tissue differentiation is correlated with decline in survival rate for individuals (Adachi et al., 2000; Jögi et al., 2012).

Furthermore, I expected a significantly greater degree of collagen disorder for moderately differentiated adenocarcinomas compared to the well differentiated group. Likewise, I also expected the poorly differentiated group to have a greater degree of disorder compared to the moderately differentiated group. These predictions were based on the reasoning that the collagen disorder is greater in more aggressive tumours to facilitate tumour cell invasion and metastasis (Piersma et al., 2020; Wu & Zhu, 2015). However, there was no significant difference in ρ between the well- and moderately-differentiated groups as well as between the moderately- and poorly-differentiated groups (Fig. 14). This emphasizes the need for future studies to investigate alternative SHG analytical techniques to quantitatively distinguish these groups from one another. In this study, I used a Gaussian function to obtain the mean ρ value from each PIPO SHG scan. As an alternative analytical approach, I can possibly compare the average number of fitted pixels with ρ values between tissue groups in a given scanning area. This alternative approach can thus indicate differences in collagen density as a measure of structural disorder.

The lack of significant differences in collagen disorder between tissue groups similar in morphological tissue architecture and cell differentiation might indicate a similar organization of collagen at the ultrastructural level in the extracellular matrix. Since the ρ structural parameter could not be used to distinguish these gastric adenocarcinoma groups, I suspect that there is little variation and disorder in the helical tilt angle of helices within collagen fibers between tissues with similar degrees of tumour aggressiveness (Tiaho et al., 2007). The implication of SHG microscopy as a diagnostic tool is that the ρ parameter is only sensitive to ultrastructural

differences between gastric adenocarcinomas that vary greatly in their degree of tumour aggressiveness.

4.3 Future Direction of Research

One of the major limitations in the study was related to the origin of the stomach tissue samples. I was unable to control how far away normal regions were sectioned from the diseased area of the stomach, since I did not perform the sectioning myself. Although having a pathological tissue slide and a normal slide allowed me to compare neoplastic and normal tissue samples from the same patients, it limited my ability to evaluate a control group of tissue samples obtained from completely unaffected organs. Despotović et al. (2020) argue that even tissue samples considered to be normal (at least 5 cm away from malignant tumours) undergo changes in the extracellular matrix. Despotović et al. (2020) used SHG microscopy to image collagen structures in normal tissue and malignant tumour regions in the colon mucosa. They observed disorderly changes in collagen organization in normal tissue obtained 10 cm and 20 cm away from the malignant tumour. This can be attributed to the systemic effects of tumours, which lead to remodelling of the extracellular matrix in distant tissues or organs (Despotović et al., 2020; McAllister & Weinberg, 2014). According to the systemic effects of tumours concept, remodelling of the ECM in distant tissue regions can be attributed to chemokines (Despotović et al., 2020; McAllister & Weinberg, 2014). Tumour cells secrete chemokines, which are signaling proteins that can mobilize host cells from distant tissue regions and modify collagen structures in the surrounding microenvironment (McAllister & Weinberg, 2014).

Given the systemic effects of tumours, this study design can be improved by performing PIPO SHG scans on a control group of normal tissue obtained from individuals with completely unaffected stomachs. Consequently, there can be further insight on collagen ultrastructure in uninvolved stomach tissue and in tumour microenvironments. I expect to see a greater difference in disorder of collagen ultrastructure (ρ) between completely uninvolved tissue regions and pathological tissue compared to normal and adjacent pathological tissues obtained from affected organs. This extension of the study is also valuable in using SHG microscopy as a quantitative method to characterize pathological stomach tissues. By determining the mean ρ value from completely unaffected tissue regions, we can assign a standard ρ value to healthy stomach tissue that pathologists can refer to when examining gastric adenocarcinomas through PSHG microscopy.

Another limitation I faced in the study was being unable to image the entire tissue core in a single PSHG scan. As outlined in the Materials and Methods section (2.2), I imaged four separate tissue regions from each tissue core with SHG microscopy. Even then, taking four separate PIPO SHG scans (each measuring 98 μm × 98 μm) did not cover large enough of an area to fully visualize collagen structures in an entire tissue core (2000 μm in diameter). I was limited in SHG imaging size because I used a laser scanning microscope set-up. In laser scanning, the laser beam is raster scanned across the sample region in a zig-zag pattern. This means that pixels are detected one by one, through the photomultiplier tube, which is a SHG signal detecting device (Zhao et al., 2019). Therefore, the slow raster scanning speed restricts us from obtaining a larger field of view of tissue cores (Zhao et al., 2019).

To overcome the limitation in sample image size, we can use a wide-field SHG microscope. Wide-field SHG set-ups do not involve raster scanning and rather require lasers with

short pulses with high energy to illuminate large sample regions (Zhao et al., 2019). A previous study achieved wide-field PSHG images that were 670 μm × 670 μm in size (Mirsanaye et al., 2022). They were able to use PSHG parameters to quantitatively compare collagen ultrastructure between normal and tumour tissue regions from the lung by analyzing the larger SHG images (Mirsanaye et al., 2022). Detecting significant differences in collagen ultrastructure between normal and pathological stomach tissue through a wide-field set-up would be hugely impactful for diagnostic applications of SHG microscopy. Since wide-field SHG microscopy can produce images of large sample regions of sectioned tissue cores, pathologists do not have to worry about selecting a limited number of small, appropriate tissue regions for observing collagen ultrastructure. This can further address concerns about accuracy in detecting overall disorderly patterns in collagen structure with the laser-scanning method. Furthermore, since wide-field microscopy produces PSHG images at a faster rate, it provides advantages in a clinical setting, in which pathologists have a limited amount of time to spare to make a final diagnosis for each patient.

4.4 Conclusions

Normal and pathological stomach tissue samples were successfully imaged using polarization-sensitive second harmonic generation microscopy. This study demonstrated that ρ can be used to distinguish collagen ultrastructure in normal stomach tissue from pathological stomach tissue, which includes well differentiated, moderately differentiated, and poorly differentiated adenocarcinomas. The results further indicated that individuals with poorly differentiated gastric adenocarcinomas are ideal candidates for distinction between normal and pathological tissue, as these two groups had the greatest difference in mean ρ values.

The significant difference in collagen ultrastructure disorder between poorly and well differentiated stomach tissue types also suggested that monitoring changes in ρ has the potential to indicate tumour aggressiveness. However, changes in ρ were not applicable in distinguishing adenocarcinomas that were similar to normal tissue in their levels of tissue differentiation. With these results in mind, the use of ρ to quantitatively characterize gastric adenocarcinomas is mainly applicable when imaging highly aggressive tumours. This finding calls for future research studies to investigate other potential parameters and analytical PSHG techniques to quantitatively distinguish various types of gastric adenocarcinomas with high confidence levels.

Overall, polarization-sensitive SHG microscopy has a promising outlook for uses as a diagnostic tool for discrimination between normal and pathological stomach tissue. SHG microscopy has applications as a complementary diagnostic tool to traditional histopathological stains, such as H&E staining. Since pathologists currently depend on qualitative observations using H&E staining, this can lead to observer bias and result in an inaccurate final diagnosis. SHG microscopy can be a viable solution to this problem because it does not require stained specimen for the observer to visualize collagen ultrastructures. If future extensions of this study can implement a wide-field SHG microscopy set-up, the process of imaging and analyzing larger stomach tissue regions can be achieved with efficacity. Analyzing structural parameters from PSHG images that represent collagen structure in large stomach tissue regions can provide pathologists with a standardized confirmatory step. Therefore, the quantitative approach that SHG microscopy can provide is powerful, as we can mitigate current issues with observer bias in histopathology.

5. References

Adachi, Y., Yasuda, K., Inomata, M., Sato, K., Shiraishi, N., & Kitano, S. (2000). Pathology and prognosis of gastric carcinoma: well versus poorly differentiated type. *Cancer*, *89*(7), 1418–1424.

Ambekar, R., Lau, T.-Y., Walsh, M., Bhargava, R., & Toussaint, K. C. (2012). Quantifying collagen structure in breast biopsies using second-harmonic generation imaging. *Biomedical Optics Express*, *3*(9), 2021–2035.

Arai, T., Matsuda, Y., Aida, J., Takubo, K., & Ishiwata, T. (2019). Solid-type poorly differentiated adenocarcinoma of the stomach: clinicopathological and molecular characteristics and histogenesis. *Gastric Cancer*, *22*(2), 314–322.

Barker, H. E., Cox, T. R., & Erler, J. T. (2012). The rationale for targeting the LOX family in cancer. *Nature Reviews Cancer*, *12*(8), 540–552.

Bordoloi, B., Siddiqui, S., Jaiswal, R., Tandon, A., Jain, A., & Chaturvedi, R. (2020). A quantitative and qualitative comparative analysis of collagen fibers to determine the role of connective tissue stroma in oral squamous cell carcinoma using special stains and polarized microscopy. *Journal of Oral and Maxillofacial Pathology*, *24*(2), 398.

Boyd, R. W. (2008). The Nonlinear Optical Susceptibility. In *Nonlinear Optics* (pp. 1–67). Elsevier.

Brittain, K., Harvey, M., Cisek, R., Pillai, S., Christie, S. D., & Tokarz, D. (2022). Second harmonic generation microscopy of otoconia. *Biomedical Optics Express*, *13*(6), 3593.

Bueno, J. M., Ávila, F. J., & Artal, P. (2017). Comparison of second harmonic microscopy images of collagen-based ocular tissues with 800 and 1045 nm. *Biomedical Optics Express*, *8*(11), 5065–5074.

Campagnola, P. (2011). Second harmonic generation imaging microscopy: applications to diseases diagnostics. *Analytical Chemistry*, *83*(9), 3224–3231.

Campagnola, P. J., & Loew, L. M. (2003). Second-harmonic imaging microscopy for visualizing biomolecular arrays in cells, tissues and organisms. *Nature Biotechnology*, *21*(11), 1356–1360.

Campagnola, P. J., Millard, A. C., Terasaki, M., Hoppe, P. E., Malone, C. J., & Mohler, W. A. (2002). Three-dimensional high-resolution second-harmonic generation imaging of endogenous structural proteins in biological tissues. *Biophysical Journal*, *82*(1 Pt 1), 493–508.

Chang, J., & Chaudhuri, O. (2019). Beyond proteases: Basement membrane mechanics and cancer invasion. *The Journal of Cell Biology*, *218*(8), 2456–2469.

Chen, X., Nadiarynkh, O., Plotnikov, S., & Campagnola, P. J. (2012). Second harmonic generation microscopy for quantitative analysis of collagen fibrillar structure. *Nature Protocols*, *7*(4), 654–669.

Cisek, R., Joseph, A., Harvey, M., & Tokarz, D. (2021). Polarization-Sensitive Second Harmonic Generation Microscopy for Investigations of Diseased Collagenous Tissues. *Frontiers in Physics*, *9*.

Courtoy, G. E., Leclercq, I., Froidure, A., Schiano, G., Morelle, J., Devuyst, O., Huaux, F., & Bouzin, C. (2020). Digital Image Analysis of Picrosirius Red Staining: A Robust Method for Multi-Organ Fibrosis Quantification and Characterization. *Biomolecules*, *10*(11).

Cox, G., Kable, E., Jones, A., Fraser, I., Manconi, F., & Gorrell, M. D. (2003). 3-dimensional imaging of collagen using second harmonic generation. *Journal of Structural Biology*, *141*(1), 53–62.

de Wever, O., Demetter, P., Mareel, M., & Bracke, M. (2008). Stromal myofibroblasts are drivers of invasive cancer growth. *International Journal of Cancer*, *123*(10), 2229–2238.

Despotović, S. Z., Milićević, Đ. N., Krmpot, A. J., Pavlović, A. M., Živanović, V. D., Krivokapić, Z., Pavlović, V. B., Lević, S., Nikolić, G., & Rabasović, M. D. (2020). Altered organization of collagen fibers in the uninvolved human colon mucosa 10 cm and 20 cm away from the malignant tumor. *Scientific Reports*, *10*(1).

Drifka, C. R., Loeffler, A. G., Mathewson, K., Mehta, G., Keikhosravi, A., Liu, Y., Lemancik, S., Ricke, W. A., Weber, S. M., Kao, W. J., & Eliceiri, K. W. (2016). Comparison of Picrosirius Red Staining With Second Harmonic Generation Imaging for the Quantification of Clinically Relevant Collagen Fiber Features in Histopathology Samples. *The Journal of Histochemistry and Cytochemistry: Official Journal of the Histochemistry Society*, *64*(9), 519–529.

Elgundi, Z., Papanicolaou, M., Major, G., Cox, T. R., Melrose, J., Whitelock, J. M., & Farrugia, B. L. (2019). Cancer Metastasis: The Role of the Extracellular Matrix and the Heparan Sulfate Proteoglycan Perlecan. *Frontiers in Oncology*, *9*, 1482.

Fischer, A., Jacobson, K. A., Rose, J., & Zeller, R. (2008). Hematoxylin and Eosin Staining of Tissue and Cell Sections. In *Basic Methods in Microscopy*. CSH Protocols.

Floyd, A. D. (2010). Evolution of Use of Special Stains. In G. Kumar & J. Kiernan (Eds.), *Special Stains and H & E* (2nd ed., pp. 39–44).

Frantz, C., Stewart, K. M., & Weaver, V. M. (2010). The extracellular matrix at a glance. *Journal of Cell Science*, *123*(24), 4195–4200.

Freund, I., Deutsch, M., & Sprecher, A. (1986). Connective tissue polarity. Optical second-harmonic microscopy, crossed-beam summation, and small-angle scattering in rat-tail tendon. *Biophysical Journal*, *50*(4), 693–712.

Fung, D. T., Sereysky, J. B., Basta-Pljakic, J., Laudier, D. M., Huq, R., Jepsen, K. J., Schaffler, M. B., & Flatow, E. L. (2010). Second harmonic generation imaging and Fourier transform spectral analysis reveal damage in fatigue-loaded tendons. *Annals of Biomedical Engineering*, *38*(5), 1741–1751.

Golaraei, A., Cisek, R., Krouglov, S., Navab, R., Niu, C., Sakashita, S., Yasufuku, K., Tsao, M.-S., Wilson, B. C., & Barzda, V. (2014). Characterization of collagen in non-small cell lung carcinoma with second harmonic polarization microscopy. *Biomedical Optics Express*, *5*(10), 3562–3567.

Golaraei, A., Kontenis, L., Cisek, R., Tokarz, D., Done, S. J., Wilson, B. C., & Barzda, V. (2016). Changes of collagen ultrastructure in breast cancer tissue determined by second-harmonic generation double Stokes-Mueller polarimetric microscopy. *Biomedical Optics Express*, *7*(10), 4054.

Golaraei, A., Mostaço-Guidolin, L. B., Raja, V., Navab, R., Wang, T., Sakashita, S., Yasufuku, K., Tsao, M.-S., Wilson, B. C., & Barzda, V. (2020). Polarimetric second-harmonic generation microscopy of the hierarchical structure of collagen in stage I-III non-small cell lung carcinoma. *Biomedical Optics Express*, *11*(4), 1851–1863.

Gole, L., Yeong, J., Lim, J. C. T., Ong, K. H., Han, H., Thike, A. A., Poh, Y. C., Yee, S., Iqbal, J., Hong, W., Lee, B., Yu, W., & Tan, P. H. (2020). Quantitative stain-free imaging and digital profiling of collagen structure reveal diverse survival of triple negative breast cancer patients. *Breast Cancer Research*, *22*(1), 42.

Green, N. H., Delaine-Smith, R. M., Askew, H. J., Byers, R., Reilly, G. C., & Matcher, S. J. (2017). A new mode of contrast in biological second harmonic generation microscopy. *Scientific Reports*, *7*(1), 13331.

Guo, Y.-T., Li, Y.-Q., Yu, T., Zhang, T.-G., Zhang, J.-N., Liu, H., Liu, F.-G., Xie, X.-J., Zhu, Q., & Zhao, Y.-A. (2008). Diagnosis of gastric intestinal metaplasia with confocal laser endomicroscopy in vivo: a prospective study. *Endoscopy*, *40*(7), 547–553.

Hase, E., Sato, K., Yonekura, D., Minamikawa, T., Takahashi, M., & Yasui, T. (2016). Evaluation of the histological and mechanical features of tendon healing in a rabbit model with the use of second-harmonic-generation imaging and tensile testing. *Bone & Joint Research*, *5*(11), 577–585.

He, L., Long, L. R., Antani, S., & Thoma, G. R. (2012). Histology image analysis for carcinoma detection and grading. *Computer Methods and Programs in Biomedicine*, *107*(3), 538–556.

Hermans, A., Kieninger, C., Koskinen, K., Wickberg, A., Solano, E., Dendooven, J., Kauranen, M., Clemmen, S., Wegener, M., Koos, C., & Baets, R. (2017). On the determination of $\chi(2)$ in thin films: a comparison of one-beam second-harmonic generation measurement methodologies. *Scientific Reports*, *7*(1), 44581.

Hristu, R., Stanciu, S. G., Dumitru, A., Eftimie, L. G., Paun, B., Tranca, D. E., Gheorghita, P., Costache, M., & Stanciu, G. A. (2022). PSHG-TISS: A collection of polarization-resolved second harmonic generation microscopy images of fixed tissues. *Scientific Data*, *9*(1), 376.

Icha, J., Weber, M., Waters, J. C., & Norden, C. (2017). Phototoxicity in live fluorescence microscopy, and how to avoid it. *BioEssays*, *39*(8).

Januszewicz, W., & Kaminski, M. F. (2020). Quality indicators in diagnostic upper gastrointestinal endoscopy. *Therapeutic Advances in Gastroenterology*, *13*(1).

Jögi, A., Vaapil, M., Johansson, M., & Påhlman, S. (2012). Cancer cell differentiation heterogeneity and aggressive behavior in solid tumors. *Upsala Journal of Medical Sciences*, *117*(2), 217–224.

Joo, M., & Han, S. H. (2016). Gastric-Type Extremely Well-Differentiated Adenocarcinoma of the Stomach: A Challenge for Preoperative Diagnosis. *Journal of Pathology and Translational Medicine*, *50*(1), 71–74.

Kalluri, R., & Zeisberg, M. (2006). Fibroblasts in cancer. *Nature Reviews Cancer*, *6*(5), 392–401.

Kardam, P., Mehendiratta, M., Rehani, S., Kumra, M., Sahay, K., & Jain, K. (2016). Stromal fibers in oral squamous cell carcinoma: A possible new prognostic indicator? *Journal of Oral and Maxillofacial Pathology : JOMFP*, *20*(3), 405–412.

Keikhosravi, A., Li, B., Liu, Y., & Eliceiri, K. W. (2020). Intensity-based registration of bright-field and second-harmonic generation images of histopathology tissue sections. *Biomedical Optics Express*, *11*(1), 160–173.

Kim, B.-M., Eichler, J., Reiser, K. M., Rubenchik, A. M., & da Silva, L. B. (2000). Collagen structure and nonlinear susceptibility: Effects of heat, glycation, and enzymatic cleavage on second harmonic signal intensity. *Lasers in Surgery and Medicine*, *27*(4), 329–335.

Kim, J. H., Kim, Y. J., An, J., Lee, J. J., Cho, J. H., Kim, K. O., Chung, J.-W., Kwon, K. A., Park, D. K., & Kim, J. H. (2014). Endoscopic features suggesting gastric cancer in biopsy-proven gastric adenoma with high-grade neoplasia. *World Journal of Gastroenterology*, *20*(34), 12233–12240.

Knoblaugh, S. E., & Randolph-Habecker, J. (2018). Necropsy and Histology. In *Comparative Anatomy and Histology* (pp. 23–51). Elsevier.

Lee, S.-H., Park, Y.-K., Cho, S.-M., Kang, J.-K., & Lee, D.-J. (2015). Technical skills and training of upper gastrointestinal endoscopy for new beginners. *World Journal of Gastroenterology*, *21*(3), 759–785.

Li, A. D., & Liu, W. C. (2010). Optical properties of ferroelectric nanocrystal/polymer composites. *Physical Properties and Applications of Polymer Nanocomposites*, 108–158.

Machlowska, J., Baj, J., Sitarz, M., Maciejewski, R., & Sitarz, R. (2020). Gastric Cancer: Epidemiology, Risk Factors, Classification, Genomic Characteristics and Treatment Strategies. *International Journal of Molecular Sciences*, *21*(11).

McAllister, S. S., & Weinberg, R. A. (2014). The tumour-induced systemic environment as a critical regulator of cancer progression and metastasis. *Nature Cell Biology*, *16*(8), 717–727.

Mirsanaye, K., Uribe Castaño, L., Kamaliddin, Y., Golaraei, A., Kontenis, L., Ẑurauskas, E., Navab, R., Yasufuku, K., Tsao, M.-S., Wilson, B. C., & Barzda, V. (2022). Unsupervised determination of lung tumor margin with widefield polarimetric second-harmonic generation microscopy. *Scientific Reports*, *12*(1).

Morgan, E., Arnold, M., Camargo, M. C., Gini, A., Kunzmann, A. T., Matsuda, T., Meheus, F., Verhoeven, R. H. A., Vignat, J., Laversanne, M., Ferlay, J., & Soerjomataram, I. (2022). The current and future incidence and mortality of gastric cancer in 185 countries, 2020–40: A population-based modelling study. *EClinicalMedicine*, *47*.

Nadiarnykh, O., LaComb, R. B., Brewer, M. A., & Campagnola, P. J. (2010). Alterations of the extracellular matrix in ovarian cancer studied by Second Harmonic Generation imaging microscopy. *BMC Cancer*, *10*(1), 94.

Ogura, Y., Tanaka, Y., Hase, E., Yamashita, T., & Yasui, T. (2019). Texture analysis of second-harmonic-generation images for quantitative analysis of reticular dermal collagen fibre in vivo in human facial cheek skin. *Experimental Dermatology*, *28*(8), 899–905.

Pantazis, P., Maloney, J., Wu, D., & Fraser, S. E. (2010). Second harmonic generating (SHG) nanoprobes for in vivo imaging. *Proceedings of the National Academy of Sciences of the United States of America*, *107*(33), 14535–14540.

Park, K. S. (2015). Introduction to Starting Upper Gastrointestinal Endoscopy: Proper Insertion, Complete Observation, and Appropriate Photographing. *Clinical Endoscopy*, *48*(4), 279–284.

Pendleton, E. G., Tehrani, K. F., Barrow, R. P., & Mortensen, L. J. (2020). Second harmonic generation characterization of collagen in whole bone. *Biomedical Optics Express*, *11*(8), 4379–4396.

Peng, L., Ran, Y.-L., Hu, H., Yu, L., Liu, Q., Zhou, Z., Sun, Y.-M., Sun, L.-C., Pan, J., Sun, L.-X., Zhao, P., & Yang, Z.-H. (2009). Secreted LOXL2 is a novel therapeutic target that promotes gastric cancer metastasis via the Src/FAK pathway. *Carcinogenesis*, *30*(10), 1660–1669.

Piersma, B., Hayward, M.-K., & Weaver, V. M. (2020). Fibrosis and cancer: A strained relationship. *Biochimica et Biophysica Acta (BBA) - Reviews on Cancer*, *1873*(2).

Rakha, E., Toss, M., & Quinn, C. (2022). Specific cell differentiation in breast cancer: a basis for histological classification. *Journal of Clinical Pathology*, *75*(2), 76–84.

Rawla, P., & Barsouk, A. (2019). Epidemiology of gastric cancer: global trends, risk factors and prevention. *Gastroenterology Review*, *14*(1), 26–38.

Rentchler, E. C., Gant, K. L., Drapkin, R., Patankar, M., & J. Campagnola, P. (2019). Imaging Collagen Alterations in STICs and High Grade Ovarian Cancers in the Fallopian Tubes by Second Harmonic Generation Microscopy. *Cancers*, *11*(11), 1805.

Roth, S., & Freund, I. (1981). Optical second-harmonic scattering in rat-tail tendon. *Biopolymers*, *20*(6), 1271–1290.

Schwartz, G. K. (1996). Invasion and metastases in gastric cancer: in vitro and in vivo models with clinical correlations. *Seminars in Oncology*, *23*(3), 316–324.

Shoulders, M. D., & Raines, R. T. (2009). Collagen structure and stability. *Annual Review of Biochemistry*, *78*, 929–958.

Simpson, G. J., & Rowlen, K. L. (1999). An SHG Magic Angle: Dependence of Second Harmonic Generation Orientation Measurements on the Width of the Orientation Distribution. *Journal of the American Chemical Society*, *121*(11), 2635–2636.

Sitarz, R., Skierucha, M., Mielko, J., Offerhaus, G. J. A., Maciejewski, R., & Polkowski, W. P. (2018). Gastric cancer: epidemiology, prevention, classification, and treatment. *Cancer Management and Research*, *10*, 239–248.

Slaoui, M., & Fiette, L. (2011). Histopathology procedures: from tissue sampling to histopathological evaluation. *Methods in Molecular Biology (Clifton, N.J.)*, *691*, 69–82.

Stoller, P., Kim, B.-M., Rubenchik, A. M., Reiser, K. M., & da Silva, L. B. (2002). Polarization-dependent optical second-harmonic imaging of a rat-tail tendon. *Journal of Biomedical Optics*, *7*(2), 205.

Sugita, S., Suzumura, T., Nakamura, A., Tsukiji, S., Ujihara, Y., & Nakamura, M. (2021). Second harmonic generation light quantifies the ratio of type III to total (I + III) collagen in a bundle of collagen fiber. *Scientific Reports*, *11*(1), 11874.

Tajiri, H., & Niwa, H. (2008). Recent Advances in Electronic Endoscopes: Image-enhanced endoscopy. *Japan Gastroenterological Endoscopy Society*, *51*(3), 199–203.

Tetreault, M.-P., & Katz, J. P. (2012). Transgenic Animal Models of Gastrointestinal Function. In *Physiology of the Gastrointestinal Tract* (pp. 97–113). Elsevier.

Tiaho, F., Recher, G., & Rouède, D. (2007). Estimation of helical angles of myosin and collagen by second harmonic generation imaging microscopy. *Optics Express*, *15*(19), 12286.

Tokarz, D., Cisek, R., Joseph, A., Asa, S. L., Wilson, B. C., & Barzda, V. (2020). Characterization of pathological thyroid tissue using polarization-sensitive second harmonic generation microscopy. *Laboratory Investigation; a Journal of Technical Methods and Pathology*, *100*(10), 1280–1287.

Tokarz, D., Cisek, R., Joseph, A., Golaraei, A., Mirsanaye, K., Krouglov, S., Asa, S. L., Wilson, B. C., & Barzda, V. (2019). Characterization of Pancreatic Cancer Tissue Using Multiphoton Excitation Fluorescence and Polarization-Sensitive Harmonic Generation Microscopy. *Frontiers in Oncology*, *9*.

Tosta, T. A. A., de Faria, P. R., Neves, L. A., & do Nascimento, M. Z. (2019). Color normalization of faded H&E-stained histological images using spectral matching. *Computers in Biology and Medicine*, *111*.

Tuer, A. E., Krouglov, S., Prent, N., Cisek, R., Sandkuijl, D., Yasufuku, K., Wilson, B. C., & Barzda, V. (2011). Nonlinear Optical Properties of Type I Collagen Fibers Studied by Polarization Dependent Second Harmonic Generation Microscopy. *The Journal of Physical Chemistry B*, *115*(44), 12759–12769.

Ushiku, T., Arnason, T., Ban, S., Hishima, T., Shimizu, M., Fukayama, M., & Lauwers, G. Y. (2013). Very well-differentiated gastric carcinoma of intestinal type: analysis of diagnostic criteria. *Modern Pathology*, *26*(12), 1620–1631.

Vanheusden, M., Vitale, R., Camacho, R., Janssen, K. P. F., Acke, A., Rocha, S., & Hofkens, J. (2020). Fluorescence Photobleaching as an Intrinsic Tool to Quantify the 3D Expansion Factor of Biological Samples in Expansion Microscopy. *ACS Omega*, *5*(12), 6792–6799.

Walker, C., Mojares, E., & del Río Hernández, A. (2018). Role of Extracellular Matrix in Development and Cancer Progression. *International Journal of Molecular Sciences*, *19*(10), 3028.

Williams, R. M., Zipfel, W. R., & Webb, W. W. (2005). Interpreting second-harmonic generation images of collagen I fibrils. *Biophysical Journal*, *88*(2), 1377–1386.

Winkler, J., Abisoye-Ogunniyan, A., Metcalf, K. J., & Werb, Z. (2020). Concepts of extracellular matrix remodelling in tumour progression and metastasis. *Nature Communications*, *11*(1).

Wu, L., & Zhu, Y. (2015). The function and mechanisms of action of LOXL2 in cancer (Review). *International Journal of Molecular Medicine*, *36*(5), 1200–1204.

Xiao, Q., & Ge, G. (2012). Lysyl oxidase, extracellular matrix remodeling and cancer metastasis. *Cancer Microenvironment : Official Journal of the International Cancer Microenvironment Society*, *5*(3), 261–273.

Yao, K. (2013). The endoscopic diagnosis of early gastric cancer. *Annals of Gastroenterology*, *26*(1), 11–22.

Yin, Y., Zhao, Y., Li, A.-Q., & Si, J.-M. (2009). Collagen: A possible prediction mark for gastric cancer. *Medical Hypotheses*, *72*(2), 163–165.

Young, E., Philpott, H., & Singh, R. (2021). Endoscopic diagnosis and treatment of gastric dysplasia and early cancer: Current evidence and what the future may hold. *World Journal of Gastroenterology*, *27*(31), 5126–5151.

Zhao, H., Cisek, R., Karunendiran, A., Tokarz, D., Stewart, B. A., & Barzda, V. (2019). Live imaging of contracting muscles with wide-field second harmonic generation microscopy using a high power laser. *Biomedical Optics Express*, *10*(10), 5130–5135.

Zhou, Z.-H., Ji, C.-D., Xiao, H.-L., Zhao, H.-B., Cui, Y.-H., & Bian, X.-W. (2017). Reorganized Collagen in the Tumor Microenvironment of Gastric Cancer and Its Association with Prognosis. *Journal of Cancer*, *8*(8), 1466–1476.

Zoumi, A., Yeh, A., & Tromberg, B. J. (2002). Imaging cells and extracellular matrix *in vivo* by using second-harmonic generation and two-photon excited fluorescence. *Proceedings of the National Academy of Sciences*, *99*(17), 11014–11019.

6. Appendices

Appendix I

Details of pathological stomach tissue cores (Slide CQ2) and their corresponding PIPO SHG scans

Tissue core # (CQ2)	Type of pathological tissue	Number of PIPO SHG scans performed	Number of PIPO SHG scans analyzed
1	Poorly differentiated adenocarcinoma	4	3
2	Poorly differentiated adenocarcinoma	4	4
3	Moderately differentiated adenocarcinoma	4	4
4	Signet ring cell carcinoma	N/A	N/A
5	Poorly differentiated adenocarcinoma	4	3
6	Poorly differentiated adenocarcinoma	4	4
7	Moderately differentiated adenocarcinoma	4	4
8	Poorly differentiated adenocarcinoma	4	1
9	Mucinous adenocarcinoma	N/A	N/A
10	Poorly differentiated adenocarcinoma	4	4
11	Moderately differentiated adenocarcinoma	4	2
12	Well differentiated adenocarcinoma	0	0
13	Signet ring cell carcinoma	N/A	N/A
14	Papillary adenocarcinoma	N/A	N/A
15	Poorly differentiated adenocarcinoma	4	2
16	Poorly differentiated adenocarcinoma	4	4
17	Poorly differentiated adenocarcinoma	4	4
18	Poorly differentiated adenocarcinoma	4	4
19	Poorly differentiated adenocarcinoma	4	3
20	Poorly differentiated adenocarcinoma	4	4
21	Poorly differentiated adenocarcinoma	4	3
22	Mucinous adenocarcinoma	N/A	N/A
23	Undifferentiated carcinoma	N/A	N/A
24	Poorly differentiated adenocarcinoma	4	4
25	Poorly differentiated adenocarcinoma	4	4
26	Mucinous adenocarcinoma	N/A	N/A
27	Well differentiated adenocarcinoma	4	4
28	Well differentiated adenocarcinoma	4	4
29	Signet ring cell carcinoma	N/A	N/A
30	Mucinous adenocarcinoma	N/A	N/A
31	Moderately differentiated adenocarcinoma	4	4
32	Moderately differentiated adenocarcinoma	4	4
33	Poorly differentiated adenocarcinoma	4	4
34	Poorly differentiated adenocarcinoma	4	4
35	Moderately differentiated adenocarcinoma	4	4

36	Poorly differentiated adenocarcinoma	0	0
37	Poorly differentiated adenocarcinoma	4	4
38	Well differentiated adenocarcinoma	4	4
39	Poorly differentiated adenocarcinoma	4	2
40	Poorly differentiated adenocarcinoma	4	4
41	Poorly differentiated adenocarcinoma	4	4
42	Moderately differentiated adenocarcinoma	4	4
43	Poorly differentiated adenocarcinoma	4	4
44	Well differentiated adenocarcinoma	4	4
45	Well differentiated adenocarcinoma	4	4
46	Signet ring cell carcinoma	N/A	N/A
47	Moderately differentiated adenocarcinoma	4	4
48	Moderately differentiated adenocarcinoma	4	4
49	Poorly differentiated adenocarcinoma	4	4
50	Moderately differentiated adenocarcinoma	0	0
51	Moderately differentiated adenocarcinoma	4	4
52	Well differentiated adenocarcinoma	4	4
53	Signet ring cell carcinoma	N/A	N/A
54	Signet ring cell carcinoma	N/A	N/A
55	Well differentiated adenocarcinoma	4	4
56	Well differentiated adenocarcinoma	0	0
57	Well differentiated adenocarcinoma	4	4
58	Signet ring cell carcinoma	N/A	N/A
59	Well differentiated adenocarcinoma	4	0

Appendix II

Details of normal stomach tissue cores (Slide CQN2) and their corresponding PIPO SHG scans

Tissue core # in CQN2 (matching patient from CQ2)	Pathological tissue type that was adjacent to normal tissue	Number of PIPO SHG scans performed	Number of PIPO SHG scans analyzed
1	Poorly differentiated adenocarcinoma	4	3
2	Poorly differentiated adenocarcinoma	4	4
3	Moderately differentiated adenocarcinoma	4	3
4	Signet ring cell carcinoma	N/A	N/A
5	Poorly differentiated adenocarcinoma	4	4
6	Poorly differentiated adenocarcinoma	4	2
7	Moderately differentiated adenocarcinoma	4	3
8	Poorly differentiated adenocarcinoma	4	3
9	Mucinous adenocarcinoma	N/A	N/A
10	Poorly differentiated adenocarcinoma	4	3
11	Moderately differentiated adenocarcinoma	0	0
12	Well differentiated adenocarcinoma	0	4
13	Signet ring cell carcinoma	N/A	N/A
14	Papillary adenocarcinoma	N/A	N/A
15	Poorly differentiated adenocarcinoma	4	4
16	Poorly differentiated adenocarcinoma	4	4
17	Poorly differentiated adenocarcinoma	4	4
18	Poorly differentiated adenocarcinoma	4	2
19	Poorly differentiated adenocarcinoma	4	3
20	Poorly differentiated adenocarcinoma	4	4
21	Poorly differentiated adenocarcinoma	0	0
22	Mucinous adenocarcinoma	N/A	N/A
23	Undifferentiated carcinoma	N/A	N/A
24	Poorly differentiated adenocarcinoma	4	4
25	Poorly differentiated adenocarcinoma	4	1
26	Mucinous adenocarcinoma	N/A	N/A
27	Well differentiated adenocarcinoma	4	4
28	Well differentiated adenocarcinoma	0	0
29	Signet ring cell carcinoma	N/A	N/A
30	Mucinous adenocarcinoma	N/A	N/A
31	Moderately differentiated adenocarcinoma	4	0
32	Moderately differentiated adenocarcinoma	4	4
33	Poorly differentiated adenocarcinoma	4	4
34	Poorly differentiated adenocarcinoma	4	3
35	Moderately differentiated adenocarcinoma	4	4
36	Poorly differentiated adenocarcinoma	4	3

37	Poorly differentiated adenocarcinoma	4	3
38	Well differentiated adenocarcinoma	0	0
39	Poorly differentiated adenocarcinoma	4	4
40	Poorly differentiated adenocarcinoma	0	0
41	Poorly differentiated adenocarcinoma	0	0
42	Moderately differentiated adenocarcinoma	4	4
43	Poorly differentiated adenocarcinoma	4	2
44	Well differentiated adenocarcinoma	4	4
45	Well differentiated adenocarcinoma	4	4
46	Signet ring cell carcinoma	N/A	N/A
47	Moderately differentiated adenocarcinoma	4	2
48	Moderately differentiated adenocarcinoma	4	3
49	Poorly differentiated adenocarcinoma	4	4
50	Moderately differentiated adenocarcinoma	4	4
51	Moderately differentiated adenocarcinoma	0	0
52	Well differentiated adenocarcinoma	0	0
53	Signet ring cell carcinoma	N/A	N/A
54	Signet ring cell carcinoma	N/A	N/A
55	Well differentiated adenocarcinoma	4	4
56	Well differentiated adenocarcinoma	4	4
57	Well differentiated adenocarcinoma	4	4
58	Signet ring cell carcinoma	N/A	N/A
59	Well differentiated adenocarcinoma	4	4